45th AIAA/ASME/SAE/ASEE Joint Propulsion Conference & Exhibit
2 - 5 August 2009, Denver, Colorado

AIAA 2009-5307

Exact Eulerian Solutions of the Cylindrical Bidirectional Vortex

Joseph Majdalani*
University of Tennessee Space Institute, Tullahoma, TN 37388

In this work, new types of Eulerian motions are investigated as potential flow candidates for describing the bidirectional vortex field in a right-cylindrical chamber. These basic solutions apply to industrial cyclone separators and to idealized representations of either liquid or hybrid rocket engines. The latter correspond to a bidirectional vortex chamber with weak sidewall permeability. As usual, we take the bulk motion to be isentropic along streamlines, with no concern for reactions, heat transfer, viscosity, compressibility, or unsteadiness. Our mathematical approach is anchored on the cylindrical Bragg-Hawthorne equation which is concurrently applied in its spherical form to the treatment of the conical cyclone (Barber, T. A., and Majdalani, J., "Exact Eulerian Solution of the Conical Bidirectional Vortex," AIAA Paper 2009-5306, August 2009). Among the unique characteristics of the new solutions, we cite the axial dependence of the swirl velocity, the Trkalian and Beltramian characters of the helical motions, the appreciable sensitivity to the outlet radius, the alternate location of the mantle, and the increased axial and radial velocity magnitudes, including the rate of mass transfer across the mantle, for which explicit approximations are obtained. Our results are compared to one another and to an existing, complex lamellar solution in which the swirl velocity collapses into a free vortex. In this vein, we find the strictly Beltramian flows to share virtually identical pressure variations and radial pressure gradients with those associated with the complex lamellar motion. By the same token, both families necessitate an asymptotic treatment to overcome their endpoint deficiencies caused by their dismissal of viscous stresses. From a broader perspective, the work delineates a logical framework through which self-similar, axisymmetric solutions to bidirectional and multidirectional vortex motions may be rigorously pursued. Furthermore, it illustrates the manner through which multiple configurations may be arrived at depending on the types of boundary conditions imposed. For example, both the slip condition at the sidewall and the inlet flow pattern at the headwall may be enforced or relaxed. Our analysis is carried out in the context of a right-cylindrical chamber first without and then with allowance for sidewall injection. The latter enables us to model the basic flow in the so-called Vortex Injection Hybrid Rocket Engine (VIHRE). Finally, the alternate mantle location and swirl velocity are verified in the light of existing measurements and numerical simulations performed with the Reynolds Stress-transport Model (RSM).

Nomenclature

A_i	=	inlet area
a	=	outer radius of the cylindrical chamber
b	=	inner radius of the circular outlet section
ψ_0	=	constant, C_1C_3
B	=	tangential angular momentum, ru_θ
c	=	constant, $1/[\beta J_1(\lambda_0\beta)] \cong 3.069148(\varepsilon = 0)$
H	=	stagnation pressure head
L	=	length of cylinder
l	=	chamber aspect ratio, L/a

*H. H. Arnold Chair of Excellence in Advanced Propulsion, Mechanical, Aerospace and Biomedical Engineering Department. Senior Member AIAA. Fellow ASME.

p	=	pressure
$\overline{p}$	=	normalized pressure, $p/(\rho U^2)$
Q_i	=	inlet volumetric flow rate, UA_i
r, z	=	radial and axial coordinates
S	=	conventional swirl number, $\pi ab / A_i = \pi\beta\sigma$
$\boldsymbol{u}$	=	velocity, (u_r, u_θ, u_z)
$\overline{\boldsymbol{u}}$	=	normalized velocity, $(u_r, u_\theta, u_z)/U$
U	=	mean tangential (inflow) velocity
U_w	=	sidewall injection velocity

Greek

β	=	open outlet fraction, b/a
β*	=	mantle location where $u_z = 0$
ε	=	sidewall injection ratio, U_w/U
κ	=	tangential inflow parameter, $(2\pi\sigma l)^{-1}$
λ_0	=	first root of $J_1(x)$, $\cong 3.83171$ $(\varepsilon = 0)$
ρ	=	density
σ	=	swirl number, a^2 / A_i
υ	=	separation constant
ψ	=	stream function

Subscripts, Symbols & Acronyms

i, o	=	inner/inlet or outer/outlet property
r, z, θ	=	radial, axial, or azimuthal component
VCCWC	=	Vortex Combustion Cold-Wall Chamber
VIHRE	=	Vortex Injection Hybrid Rocket Engine

I. Introduction

CYCLONIC motions pertain to a number of vortex-fired engine technologies including such devices as the Vortex Hybrid Engine introduced by Gloyer, Knuth and Goodman,[1] the Vortex Injection Hybrid Rocket Engine conceived by Knuth *et al.*,[2] the Vortex Combustion Cold-Wall Chamber developed by Chiaverini *et al.*,[3] and the Reverse Vortex Combustor spawned by Matveev *et al.*[4] In addition to their propulsive function, these fascinating swirl-induced patterns are inherently connected to meteorological phenomena such as tornadoes, hurricanes, dustdevils, and typhoons;[5] astrophysical activities of cosmic spirals, galactic pinwheels, and helical trajectories of celestial bodies;[6-7] and industrial processes employing cyclonic separators, combustors, and furnaces.[8]

For the cylindrical cyclone, some of the earliest laboratory investigations point us to ter Linden[9] whose efforts to characterize dust separation efficiency were swiftly succeeded by the classical experiments on hydraulic and gas cyclones reported by Kelsall[10] and Smith.[11-12] These fundamental experiments suggested the existence of forced, rather than free vortex behavior in the core region of a cyclone. Other theoretical studies of hydraulic cyclones emerged but these were chiefly based on semi-empirical methods.[13] Among them stood the Polhausen technique which was introduced in this context[14] and later traded by Bloor and Ingham[15] for an Eulerian approach to the treatment of a conical cyclone. With the widespread use of computational alternatives, shortly after Bloor and Ingham's work, mathematical modeling seems to have suddenly fallen out of favor in exchange for two- and three-dimensional simulations of cyclonic devices. Several experimental and numerical investigations have since been carried out including those by Hsieh and Rajamani,[16] Hoekstra *et al.*,[17] Hoekstra, Derksen and Van den Akker,[18] Derksen and Van den Akker,[19] Fang, Majdalani and Chiaverini,[20] Rom, Anderson and Chiaverini,[21] Murray *et al.*,[22] Hu *et al.*,[23] Zhiping, Yongjie and Qinggand,[24] and Molina *et al.*[25] In retrospect, an extensive survey on this subject by Cortes and Gil[26] unequivocally affirms that most realistic mean flow models of cyclone separators remain empirical in nature and, in actuality, firmly reliant on least-squares and curve fitting techniques. As for the numerical simulations carried out so far, most seem to be turbulence-model dependent and, in their own way, limited in their ability to furnish universal predictions. More significantly perhaps, their results seem to falter in providing deeper physical insight than may be retrieved from a well-posed theoretical framework.

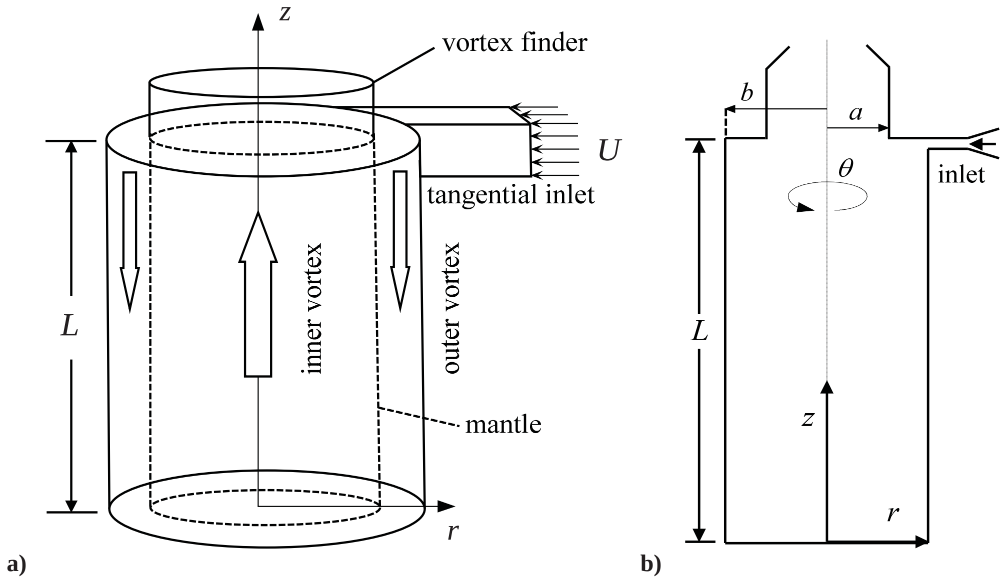

Figure 1. Schematic of a cylindrical cyclonic chamber showing a) separate vortex regions and b) coordinate system used.

Given the shortage of purely analytical models of axisymmetric cyclonic flows,[27] an Eulerian based solution was developed by Vyas, Majdalani and Chiaverini[28] for a right-cylindrical VCCWC chamber model. Although their effort only produced a simple solution for the problem at hand,[29] it set the pace for a laminar boundary layer treatment of the viscous core[30] along with a cursory characterization of the multiple-mantle paradigm.[31] Shortly thereafter, the extension to the hybrid vortex configuration was conceived and carried out by Majdalani and Vyas,[32] and later refined by Majdalani.[33] As for the sidewall boundary layers, they were resolved under laminar conditions by Vyas and Majdalani[34] and then, for the axial and radial orientations, by Batterson and Majdalani.[35] Meanwhile, despite this incremental progress, the analytical treatment of the core region remained, effectively, incomplete. This was especially true at high Reynolds numbers for which the aforementioned (laminar) profiles overpredicted the maximum swirl velocity. To partly address this issue, Maicke and Majdalani[36] applied a turbulence-based, constant shear stress model to the core region from which they extracted a piecewise, Rankine-like approximation for the swirl velocity. In the same article, it was shown that the use of a higher effective turbulent eddy viscosity in the calculation of the vortex Reynolds number could lead to satisfactory alignment with experimental measurements.

In the interim, realizing the need to explore other potential candidates to this problem, Majdalani and Rienstra[37] turned their attention to the general vorticity equation in spherical coordinates. This step, which was initiated in 2004,[38] allowed them to identify uniform, linear and nonlinear classes of exact Eulerian solutions for problems with constant angular momentum. These were classified according to the relation established between their tangential mean flow vorticity ω_θ and their stream function ψ. Their type I representation displayed uniform vorticity and reproduced, in one case, the potential flow past a sphere (i.e., the external portion of Hill's spherical vortex[39]). Their type II solution assumed a linear relation $\omega \sim \psi$ and reproduced, in one situation, the bidirectional vortex in a cylindrical chamber.[29] Finally, their type III considered nonlinear relations of the form $\omega \sim \psi^q; q \neq (0,1)$. These representations gave rise to interesting flow patterns that could be computed numerically for $q \neq (-3,0,1)$ or extracted analytically for $q = -3$.

In seeking additional types of solutions that are recoverable from the spherical Bragg-Hawthorne equation (BHE),[40] Barber and Majdalani[41] revisited the conical cyclonic flow problem that was first considered by Bloor and Ingham.[15] Their analysis led to a portable, self-similar, verifiable solution that is independent of the cone's finite body length. It also gave rise to explicit approximations of several flow attributes such as the mantle location, maximum chamber velocities and their loci, and both pressure and vorticity distributions. Moreover, it permitted the identification of the basic forms of the angular momentum relation to the stream function and to the procedural steps required to (i) account for the spatial variance of the swirl velocity and (ii) capture the effects of a specific injection flow pattern. In this companion article, a similar procedure is implemented in the context of axisymmetric cyclonic flow in a cylindrical chamber. In this vein, both hard and permeable wall conditions will be considered, with the latter posing an idealized representation for the internal flowfield of a Vortex Injection Hybrid Rocket Engine.

II. Formulation

A. Cylindrical Bragg-Hawthorne Equation

The procedure used by Barber and Majdalani[41] may be judiciously extended to the analogous problem arising in a confined cylinder (see Fig. 1a). The corresponding study was previously explored via the vorticity-stream function approach by Vyas and Majdalani,[29] Majdalani and Rienstra,[37] and, most recently, by Maicke and Majdalani.[36] Starting with the cylindrical BHE expression,[42] one can put

$$\frac{\partial^2\psi}{\partial r^2}-\frac{1}{r}\frac{\partial\psi}{\partial r}+\frac{\partial^2\psi}{\partial z^2}=r^2\frac{\mathrm{dH}}{\mathrm{d}\psi}-\mathrm{B}\frac{\mathrm{dB}}{\mathrm{d}\psi} \tag{1}$$

where $\mathrm{B}=ru_\theta$ and $\mathrm{H}=p/\rho+\boldsymbol{u}\cdot\boldsymbol{u}/2$ denote the tangential angular momentum and the total pressure head, respectively.[40] Everywhere, the nomenclature and conditions used by Majdalani and Rienstra[37] are adhered to as closely as possible (see Fig. 1b).

It may be instructive to note that Eq. (1) may be linearized by choosing conditions leading to a simple right-hand-side that renders either a constant, as in the case of Bloor and Ingham,[15] or a linear function of ψ, as in the case of Vyas and Majdalani.[29] Such conditions arise when B is either constant or

$$\begin{cases}\mathrm{B}\dfrac{\mathrm{dB}}{\mathrm{d}\psi}=\text{const}\\[2ex] \mathrm{B}\dfrac{\mathrm{dB}}{\mathrm{d}\psi}\sim\psi\end{cases}\qquad \begin{cases}\mathrm{B}=\sqrt{B_0\psi+B_1} & (a)\\ \mathrm{B}=\sqrt{B_0\psi^2+B_1} & (b)\end{cases} \tag{2}$$

and H has to simultaneously be either constant or

$$\begin{cases}\dfrac{\mathrm{dH}}{\mathrm{d}\psi}=\text{const}\\[2ex] \dfrac{\mathrm{dH}}{\mathrm{d}\psi}\sim\psi\end{cases}\qquad \begin{cases}\mathrm{H}=H_0\psi & (a)\\ \mathrm{H}=H_0\psi^2+H_1 & (b)\end{cases} \tag{3}$$

For example, in the development of the sinusoidal predecessor model, Vyas and Majdalani[29] have implicitly used $\mathrm{B}(\psi)=1, \mathrm{dB}/\mathrm{d}\psi=0$ and $\mathrm{d}H/\mathrm{d}\psi=-C_n^2\psi,$ to the extent of producing a linear BHE. Presently, this order will be reversed as we follow Bloor and Ingham[15] and assume isentropic conditions that permit setting $\mathrm{d}H/\mathrm{d}\psi=0.$ Moreover, we seek a slight generalization by granting the angular momentum dependence on the stream function,

$$B(\psi)=ru_\theta=\sqrt{B_0\psi^2+B_1} \tag{4}$$

For simplicity, we take $B_0=C_n^2$ and put

$$\mathrm{B}\frac{\mathrm{dB}}{\mathrm{d}\psi}=C_n^2\psi \tag{5}$$

where C_n^2 denotes some constant that needs to be determined from suitable boundary conditions. Inserting Eq. (5) into the Bragg-Hawthorne equation, one obtains

$$\frac{\partial^2\psi}{\partial r^2}-\frac{1}{r}\frac{\partial\psi}{\partial r}+\frac{\partial^2\psi}{\partial z^2}+C_n^2\psi=0 \tag{6}$$

which resembles the equation solved by Vyas and Majdalani[29] except for the absence of an r^2 multiplying the last member of Eq. (6). As usual, one may assume $\psi(r,z)=f(r)g(z)$ and transform Eq. (6) into

$$-\frac{\ddot g(z)}{g(z)}=\frac{1}{f}\left(f''-\frac{1}{r}f'+C_n^2 f\right)=\begin{cases}0\\ +\upsilon^2\\ -\upsilon^2\end{cases} \tag{7}$$

Three solutions arise and these depend on the choice of the separation constant:

$$\psi(r,z)=\begin{cases} r(C_1z+C_2)\left[C_3J_1(C_nr)+C_4Y_1(C_nr)\right]; & \upsilon=0\\ r\left[C_1\sin(\upsilon z)+C_2\cos(\upsilon z)\right]\left[C_3J_1(r\sqrt{C_n^2-\upsilon^2})+C_4Y_1(r\sqrt{C_n^2-\upsilon^2})\right]; & C_n^2>\upsilon^2\\ r\left[C_1\sinh(\upsilon z)+C_2\cosh(\upsilon z)\right]\left[C_3J_1(r\sqrt{C_n^2+\upsilon^2})+C_4Y_1(r\sqrt{C_n^2+\upsilon^2}\right] \end{cases} \tag{8}$$

For the bidirectional motion in a cylinder, an assortment of constraints may be imposed, specifically[37]

$$\begin{cases} z=0; \quad u_z(r,0)=0; \quad \partial\psi/\partial r=0 & \text{(a)} \\ r=0; \quad u_r(0,z)=0; \quad \partial\psi/\partial z=0 & \text{(b)} \\ r=a; \quad u_r(a,z)=0; \quad \partial\psi/\partial z=0 & \text{(c)} \end{cases} \tag{9}$$

As for the sidewall condition on u_θ, two conditions may be systematically considered. The first enforces a zero tangential velocity at the wall, $u_\theta(a,z)=0$, whereas the second matches the outer circumferential velocity to the maximum swirl speed at entry, $u_\theta(a,z)=U$. The outcome of each of these assumptions will be discussed below. Furthermore, the $\upsilon=0$ case will constitute our chief focus while the remaining two cases, which give rise to sinusoidal or exponential variations in z, will be evaluated separately. Before concluding our analysis, the case of sidewall injection will be considered and resolved, being a special case of the problem at hand.

B. Similarity Conforming Solutions

The first condition in Eq. (9) requires the vanishing of the axial velocity at the headwall or $C_2=0$. Along similar lines, one must set $C_4=0$ to suppress the unbounded behavior of the radial velocity at the centerline. This leaves us with $\psi=\psi_0 z\, rJ_1(C_n r)$, where $\psi_0 \equiv C_1C_3$. The third condition yields

$$J_1(C_n a)=0 \qquad C_n=\frac{\lambda_n}{a}; n=0,1,2 \tag{10}$$

where $\lambda_n=(3.83171, 7.01559, 10.1735, 13.3237, ...)$ denote the roots of the Bessel function of the first kind. For a single turning point behavior, one takes $C_0=\lambda_0/a=3.83171/a$, $\psi=\psi_0 z\, rJ_1(\lambda_0 r/a)$, and puts

$$\boldsymbol{u}=-\psi_0 J_1\left(\lambda_0\frac{r}{a}\right)\boldsymbol{e}_r+\frac{1}{r}\left[\psi_0^2\lambda_0^2 r^2\left(\frac{z}{a}\right)^2 J_1^2\left(\lambda_0\frac{r}{a}\right)+B_1\right]^{1/2}\boldsymbol{e}_\theta+\psi_0\frac{z}{a}\lambda_0 J_0\left(\lambda_0\frac{r}{a}\right)\boldsymbol{e}_z \tag{11}$$

The constant ψ_0 may be secured from a global mass balance. At steady state, a volumetric rate of $Q_i=UA_i$ entering the chamber must exit through the downstream opening of radius b. This enables us to write

$$2\pi\int_0^b \boldsymbol{u}\cdot\hat{\boldsymbol{n}}\; r\mathrm{d}r=2\pi\int_0^b u_z(r,L)\, r\mathrm{d}r=Q_i \tag{12}$$

and deduce

$$\psi_0=\frac{Q_i}{2\pi a\beta L J_1(\lambda_0\beta)} \tag{13}$$

where $\beta=b/a$ is the open fraction of the radius at $z=L$.

At this stage, one of two boundary conditions may be used for the tangential velocity. By analogy with the Taylor-Culick inviscid profile that self-satisfies the no-slip at the wall, we first attempt to impose, $u_\theta(a,z)=0$, or $B_1=0$. The problem simplifies considerably with the elimination of the leading r^{-1} term and the attendant singularity at the centerline. We are left with

$$u_\theta=\psi_0\lambda_0\left(\frac{z}{a}\right)J_1\left(\lambda_0\frac{r}{a}\right) \tag{14}$$

C. Normalization

Using the standard reference values introduced by Majdalani and Rienstra,[37] we put

$$\begin{cases} \bar{r}=\dfrac{r}{a}, \quad \bar{z}=\dfrac{z}{a}, \quad \bar{u}_r=\dfrac{u_r}{U}, \quad \bar{u}_\theta=\dfrac{u_\theta}{U}, \quad \bar{u}_z=\dfrac{u_z}{U} \\ \bar{p}=\dfrac{p}{\rho U^2}, \quad \bar{\psi}=\dfrac{\psi}{Ua^2}, \quad \bar{\mathrm{B}}=\dfrac{\mathrm{B}}{aU}, \quad \bar{Q}_i=\dfrac{Q_i}{Ua^2}=\dfrac{A_i}{a^2}=\sigma^{-1} \end{cases} \tag{15}$$

The normalized velocity becomes

$$\bar{\boldsymbol{u}}=-\frac{\psi_0}{U}J_1(\lambda_0\bar{r})\boldsymbol{e}_r+\frac{\lambda_0\psi_0}{U}\bar{z}J_1(\lambda_0\bar{r})\boldsymbol{e}_\theta+\frac{\lambda_0\psi_0}{U}\bar{z}J_0(\lambda_0\bar{r})\boldsymbol{e}_z \tag{16}$$

which, by way of Eq. (13), renders,

$$\bar{\boldsymbol{u}}=-\frac{1}{2\pi\sigma l}\frac{J_1(\lambda_0\bar{r})}{\beta J_1(\lambda_0\beta)}\boldsymbol{e}_r+\frac{1}{2\pi\sigma l}\lambda_0\bar{z}\frac{J_1(\lambda_0\bar{r})}{\beta J_1(\lambda_0\beta)}\boldsymbol{e}_\theta+\frac{1}{2\pi\sigma l}\lambda_0\bar{z}\frac{J_0(\lambda_0\bar{r})}{\beta J_1(\lambda_0\beta)}\boldsymbol{e}_z$$

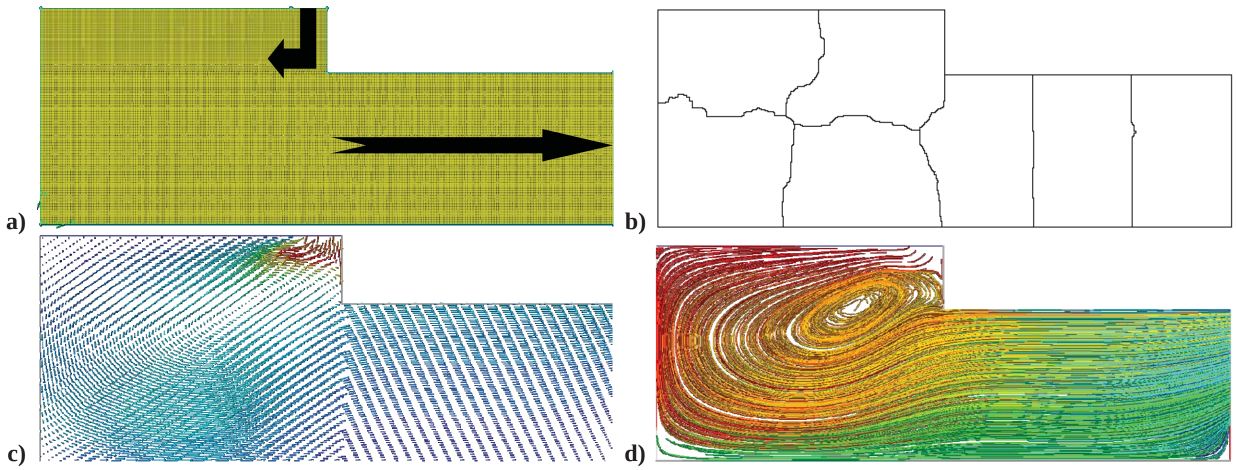

Figure 2. Computational domain used in the axisymmetric RSM simulation of a vortex tank with detail on a) quadrilateral mesh distribution, b) zone partitioning, c) vector plots, and d) streamlines.

$$= -\kappa \frac{J_1(\lambda_0 \bar{r})}{\beta J_1(\lambda_0 \beta)} \boldsymbol{e}_r + \lambda_0 \kappa \bar{z} \frac{J_1(\lambda_0 \bar{r})}{\beta J_1(\lambda_0 \beta)} \boldsymbol{e}_\theta + \lambda_0 \kappa \bar{z} \frac{J_0(\lambda_0 \bar{r})}{\beta J_1(\lambda_0 \beta)} \boldsymbol{e}_z \tag{17}$$

and

$$\bar{\psi} = \kappa \bar{z}\, \bar{r} \frac{J_1(\lambda_0 \bar{r})}{\beta J_1(\lambda_0 \beta)} \tag{18}$$

where $\kappa \equiv (2\pi\sigma l)^{-1} = A_i / (2\pi a L) = 0.35355 a / (SL)$, and $S = \left(\pi / \sqrt{2}\right)\sigma \cong 2.22\sigma$ is the standard swirl number. Equation (17) encapsulates one type of behavior that may be associated with the resulting stream function. However, the dependence of its swirl velocity, $\bar{u}_\theta$, on the reciprocal of the swirl number, through $\kappa \sim \sigma^{-1} l^{-1}$, is not expected. While we continue to study the behavior of Eq. (17), we are inclined to search for other possible forms that arise when using different inlet and wall boundary conditions. Additionally, the axial variation of the stream function will be studied in view of the trigonometric types of solutions given by Eq. (8). Some of these will be expounded below.

D. Reynolds Stress-transport (RSM) Simulation

A simplistic simulation of the cylindrical chamber is carried out using the "vortex tank" shown in Fig. 2. Using SI units everywhere, the tank is created with $L = 0.2$, $a = 0.15$, and an outlet radius of $b = 0.105$. The tubular vortex finder that is attached at $z = L$ extends an equal distance downstream. This is performed to aid in flow development. Air with density $\rho = 1.225$, $\mu = 1.7894 \times 10^{-5}$, and a circumferential injection velocity of $U = 260$ is applied as an inlet velocity condition along a segment of length $L_i = 0.025$. The inlet velocity is slanted at 7 degrees inward from the purely tangential direction, thus granting it an effective tangential component of 258 m/s and a small radial contribution of 31.7 m/s. The total inlet area is hence $A_i = 2\pi a L_i = 0.02356$. The sidewall velocity is denoted by U_w and can be varied from zero to a value that is characteristic of hybrid propellant burning. Taking advantage of axisymmetry, a two-dimensional double precision simulation is initiated with the Realizable $k-\varepsilon$ (RKE) model because of its convergence properties. The model is later switched to RSM because of its enhanced suitability for the treatment of swirl-dominated flows.[43] Our mesh consists of 90,580 quadrilateral cells organized into 7 partitions that are synchronously extruded along the chamber. Grid refinement is carried out to ensure grid convergence. Our physical properties correspond to an aspect ratio of $l = \frac{4}{3} = 1.333$, an open fraction of $\beta = 0.7$, a kinematic viscosity of $\nu = 1.46 \times 10^{-5}$, a normalized volumetric flow rate $Q_i = A_i / a^2 = 1.047$, and a tangential inflow parameter of $\kappa = 0.125$.

Regarding the choice of a solver, our code is based on the Finite Volume Method (FVM). FVM pertains to the discretization scheme applied to the governing PDEs and is particularly suited to those arising in fluid and mass transport problems.[44] Accordingly, the general PDE controlling the flux of a conserved passive scalar can be written as

$$\underbrace{\partial(\rho\phi)/\partial t}_{\text{unsteady}} + \underbrace{\nabla \cdot (\rho \boldsymbol{u} \phi)}_{\text{convection}} = \underbrace{\nabla \cdot (\Gamma \nabla \phi)}_{\text{diffusion}} + \underbrace{S_\phi}_{\text{source}} \tag{19}$$

where ρ, t, $\boldsymbol{u}$, Γ, and ϕ denote the density, time, velocity, diffusivity, and the unknown scalar for which we seek a solution. FVM requires integrating over each of the domain control volumes; this operation yields an algebraic equation relating neighboring values of the dependent variables to the centroidal nodes of each control volume.[45] The resulting algebraic expression, for a control volume P, takes the form

$$a_P \phi_P + \sum_{i=N_P} a_{N_i} \phi_{N_i} = b_P \tag{20}$$

where $N_i = 1, 2, \ldots, N_P$ represent the neighboring cells. The coefficients depend on the specific interpolation scheme used in the discretization process. Upwind and QUICK schemes are used, for example, to relate face values to control volume values in the convective terms. In our simulations, we employ first order schemes for all terms and the SIMPLE algorithm to resolve the pressure and velocity coupling.[44-45]

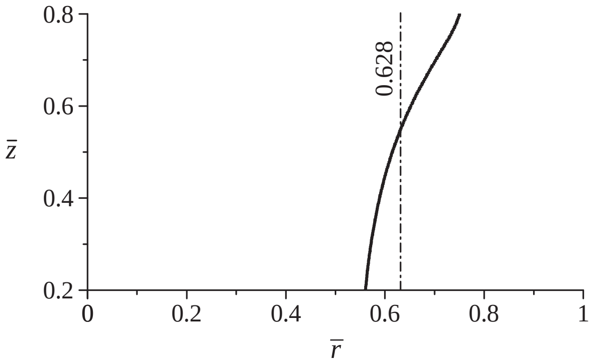

Figure 3. Mantle location according to the RSM simulation of the vortex tank shown in Fig. 2.

III. Fundamental Characteristics

A. Theoretical Locations of the Mantle

The cylindrical mantle or spinning wheel refers to the axially rotating layer that separates the updraft (or inner vortex) from the downdraft (or outer vortex). Along this surface, one may set $u_z = 0$ and solve for the corresponding radial position $r = \beta^*$. One readily obtains $J_0(\lambda_0 \beta^*) = 0$ or $\beta^* = 0.627612$. This result is quite intriguing as it differs from the 0.707 value obtained previously by Vyas and Majdalani.[29] Nonetheless, it seems to fall closer to the recent CFD simulation carried out in house using a right-cylindrical chamber (see Fig. 3). It also stands more or less in line with the average value of $\beta^* \cong 0.675$ predicted by Hoekstra, Derksen and Van Den Akker,[18] although theirs

Table 1. Experimental mantle location according to Smith[11-12]

Site	Position	Case I (2″ inlet)		Case II (0.5″ inlet)	
No.	$L-\bar{z}$ [in]	$\bar{r}$ [in]	β^*	$\bar{r}$ [in]	β^*
1	0.0	1.99	0.6633	2.13	0.7083
2	1.5	1.89	0.6300	2.15	0.7166
3	3.0	1.88	0.6266	2.15	0.7166
4	4.5	1.85	0.6166	2.15	0.7166
5	6.0	1.79	0.5966	2.17	0.7233
6	7.5	1.79	0.5966	2.20	0.7333
7	9.0	1.75	0.5833	2.20	0.7333
Mean		1.85	0.6166	2.16	0.7211

Table 2. Matrix of mantle locations

m	$n=1$	$n=2$	$n=3$	$n=4$	$n=5$
1	$\beta_{1,1} = 0.6276$				
2	$\beta_{2,1} = 0.342783$	$\beta_{2,2} = 0.786831$			
3	$\beta_{3,1} = 0.236382$	$\beta_{3,2} = 0.542596$	$\beta_{3,3} = 0.850617$		
4	$\beta_{4,1} = 0.180492$	$\beta_{4,2} = 0.414305$	$\beta_{4,3} = 0.649499$	$\beta_{4,4} = 0.885005$	
5	$\beta_{5,1} = 0.146007$	$\beta_{5,2} = 0.335147$	$\beta_{5,3} = 0.525404$	$\beta_{5,4} = 0.715913$	$\beta_{5,5} = 0.906518$

remains closer to 0.707 than 0.628. Note that these researchers' experimental and numerical tests were carried out at a moderate Reynolds number of $Re = 5\times10^4$ and three decreasing swirl numbers of $S = 3.1$, 2.2 and 1.8.[18] The small deviations from our predicted value may be attributed to their specific use of a Reynolds stress transport model and to inevitable differences that are germane to industrial gas cyclones. In comparison to other investigations of cylindrical cyclones, the most notable may be the classical experiments by J. L. Smith who studied, with the aid of smoke, the formation of laminar vortex structures in a right-cylindrical cyclone that comprised a flat bottom and a vortex finder.[11-12] Based on the two test cases reported in Smith's work, the experimental mantle measurements are catalogued in Table 1 at several axial positions. It is gratifying that not only do his values exhibit weak sensitivity to the distance from the headwall, but they also corroborate the duality of roots obtained so far with his averages falling around 0.62 and 0.72. Concerning the weak sensitivity of mantle excursions to inlet flow conditions, confirmatory studies have been reported separately by Vatistas, Lin and Kwok[46-47] and, by in-house studies including those by Fang, Majdalani and Chiaverini.[20,48] As for the possibility of inception of multidirectional flow passes, the corresponding mantle locations stem from Eq. (10) and are summarized in Table 2.

B. Characteristic Properties

To avoid corner collisions in the exit plane, the chamber opening may be taken such that the open fraction is set to coincide with the mantle location, $\beta = \beta^* = 0.627612$. By aligning the outflow diameter with the opening at $\bar{z} = l$, undesirable flow circulation and secondary flow formation may be mitigated. The optimal solution simplifies into

$$\begin{aligned}\bar{\psi} &= c\kappa\bar{z}\,\bar{r}J_1(\lambda_0\bar{r}) = 3.069\kappa\bar{z}\,\bar{r}J_1(\lambda_0\bar{r})\\ \bar{\boldsymbol{u}} &= -c\kappa J_1(\lambda_0\bar{r})\boldsymbol{e}_r + c\lambda_0\kappa\bar{z}J_1(\lambda_0\bar{r})\boldsymbol{e}_\theta + c\lambda_0\kappa\bar{z}J_0(\lambda_0\bar{r})\boldsymbol{e}_z\\ &= -3.069\kappa J_1(\lambda_0\bar{r})\boldsymbol{e}_r + 11.76\kappa\bar{z}J_1(\lambda_0\bar{r})\boldsymbol{e}_\theta + 11.76\kappa\bar{z}J_0(\lambda_0\bar{r})\boldsymbol{e}_z\end{aligned} \tag{21}$$

where $c \equiv 1/[\beta J_1(\lambda_0\beta)]$ in general, and $c = 3.069148$ for the particular case of $\beta = \beta^*$. From this expression, the radial crossflow velocity along the mantle may be calculated to be:

$$(\bar{u}_r)_{\text{cross}} = -1.59334\kappa \tag{22}$$

which is 12.7% larger than the previously estimated value of $(\bar{u}_r)_{\text{cross}} = -1.41421\kappa, \forall \bar{z}$ (cf. Vyas and Majdalani[29]).

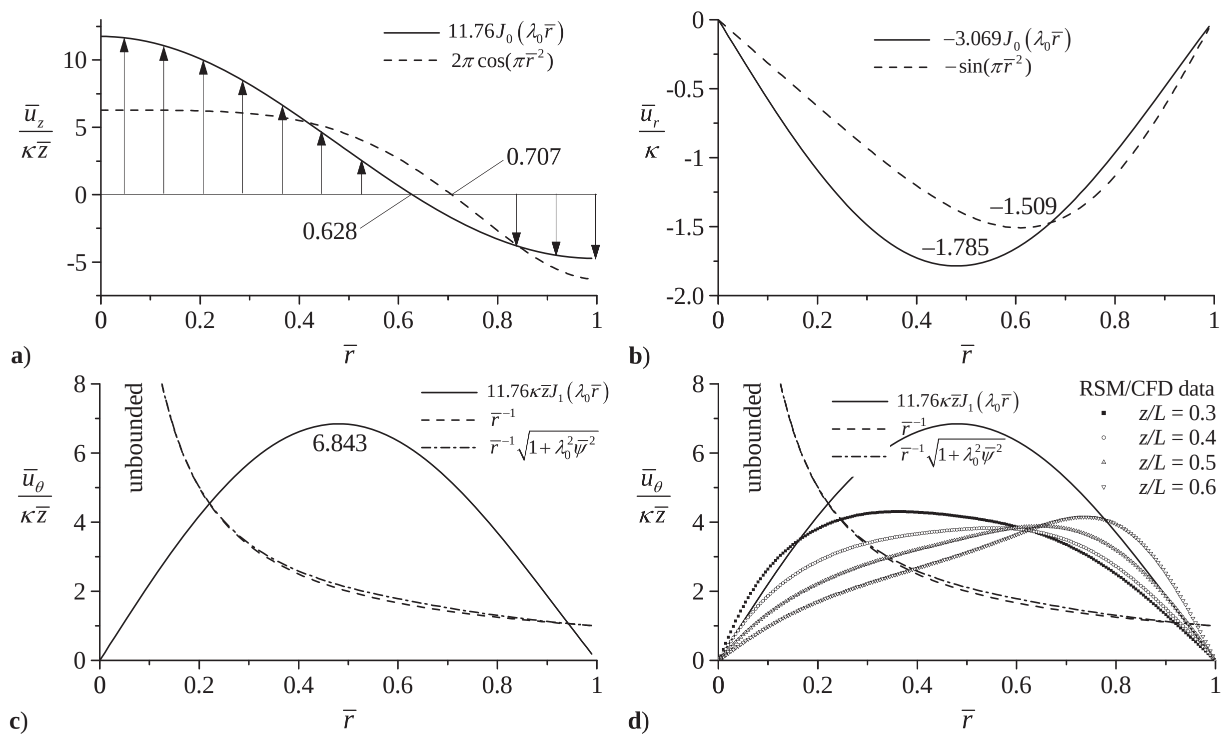

Figure 4. Comparisons for a) axial, b) radial, and c) tangential velocity distributions. We show in d) CFD data based on the RSM model.

Furthermore, a simple check of $2\pi\beta l\left|(\bar{u}_r)_{\text{cross}}\right| = \bar{Q}_i$ confirms that the entire mass entering the chamber is transported from the annular region into the inner vortex, uniformly along the mantle, before exiting at $\bar{z} = l$. Interestingly, both tangential and radial velocities reach their peak magnitudes at the same $\bar{r}_{\max}$ which, in turn, can be computed from

$$J_0(\lambda_0 \bar{r}_{\max}) - J_2(\lambda_0 \bar{r}_{\max}) = 0 \tag{23}$$

Thus for $\bar{r}_{\max} = 0.480513$ we find $(\bar{u}_r)_{\max} = -1.78583\kappa$ to be comparable in size to the previously reported value[29] of -1.50879κ. As for the tangential velocity, its maximum is no longer infinite but rather prescribed by the location and inflow parameter: $(\bar{u}_\theta)_{\max} = 6.84278\kappa\bar{z}$. This result is interesting as it suggests that $\bar{u}_\theta$, in its purely inviscid form, may be non-singular along the axis of rotation. However, the inverse dependence of $(\bar{u}_\theta)_{\max}$ on the swirl number, through $\kappa \sim \sigma^{-1} l^{-1}$, leads to a fundamental paradox that we hope to resolve in later study.

In the interest of clarity, normalized forms of the axial, radial, and tangential velocities are presented in Fig. 4 where they are also compared to the trigonometric profile derived by Vyas and Majdalani,[29]

$$\bar{\boldsymbol{u}} = -\kappa\bar{r}^{-1}\sin(\pi\bar{r}^2)\boldsymbol{e}_r + \bar{r}^{-1}\boldsymbol{e}_\theta + 2\pi\kappa\bar{z}\cos(\pi\bar{r}^2)\boldsymbol{e}_z \tag{24}$$

In hindsight, this solution belongs to the family of complex lamellar flows[49] for which streamlines remain everywhere perpendicular to vorticity lines by virtue of their vanishing helicity density, $\bar{\boldsymbol{\omega}} \cdot \bar{\boldsymbol{u}} = 0$. Furthermore, Eq. (24) can be directly retrieved from Eq. (1) by setting $\mathrm{B} = aU$ and $\mathrm{d}H/\mathrm{d}\psi = -C_n^2\psi$. As before, the axial velocity shown in Fig. 4a varies linearly with $\bar{z}$, from a vanishingly small value at the headwall to a maximum that occurs at the center of the exit plane. In relative comparison to the sinusoidal solution, the centerline velocity amplification ascribed to the present model may be readily deduced from $11.76 J_0(0)/\left[2\pi\cos(0)\right] = 1.872$.

Surely, the 87% amplification in the maximum axial velocity may be surmised from the graph. As for the radial velocity magnitude, it vanishes at the sidewall and increases inwardly, thus peaking shortly after crossing the mantle, halfway along the radius ($\bar{r}_{\max} = 0.480513$). Subsequently, $|\bar{u}_r|$ decreases until it fully disappears along $\bar{r} = 0$ (see Fig. 4b). The comparison for the self-similar swirl velocity is showcased in Fig. 4c side-by-side with the free vortex expression.[29] While the latter remains insensitive to $\kappa\bar{z}$, the present model varies with the axial position and the tangential inflow parameter, thus peaking in the exit plane. It also comprises two evenly balanced regions that are somewhat reminiscent of the forced and free vortex regions except for the relative size of the forced vortex which is traditionally the smaller of the two. In relation to the RSM data shown in Fig. 4d, $(\bar{u}_\theta)_{\max}$ seems to slightly

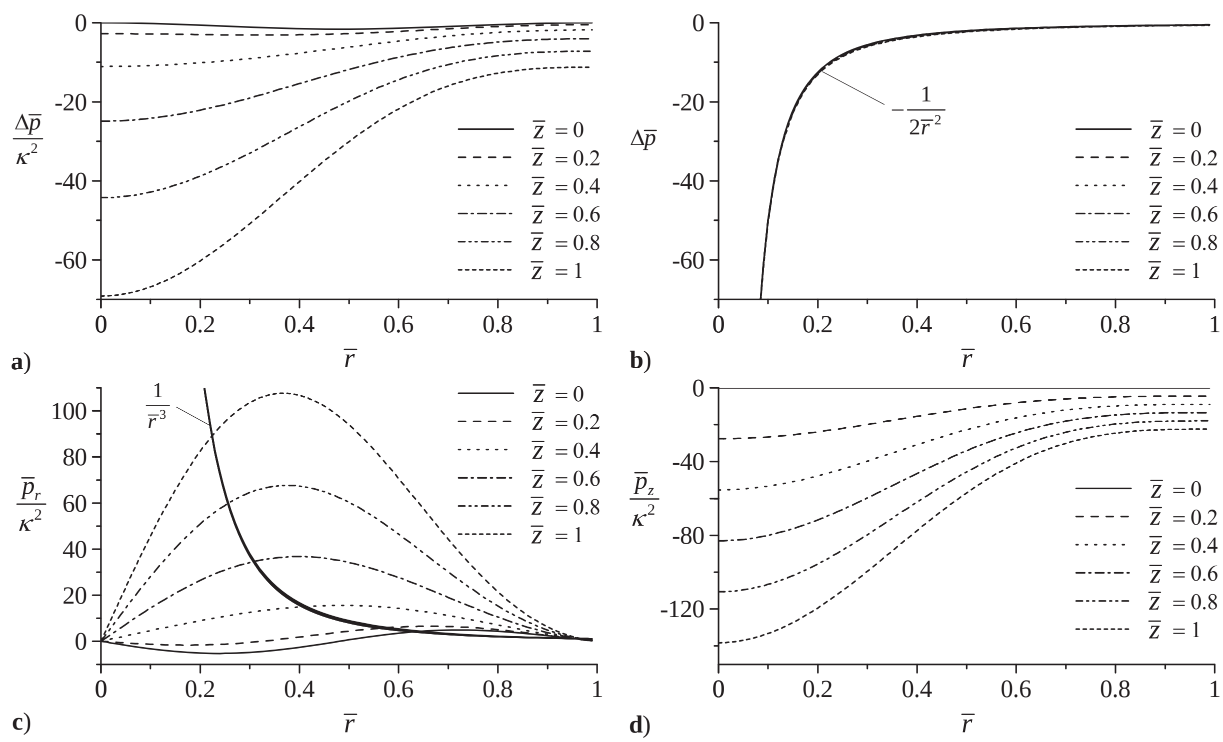

Figure 5. Pressure differential for a) slip resistant and b) slip permitting cases. Corresponding radial and axial pressure gradients are shown in c-d) at several axial positions. Both solutions share the same axial pressure gradient.

overpredict the maximum swirl detected at four axial positions. This behavior can be attributed to the present model being purely inviscid and to viscous stresses constituting an important damping agent that cannot be captured here.

Having briefly sketched the velocities, the pressure gradients that accompany them may be obtained directly from Euler's equations viz.

$$\frac{\partial \bar{p}}{\partial \bar{r}} = c^2\kappa^2\left[\frac{(1+\lambda_0^2\bar{z}^2)}{\bar{r}}J_1^2(\lambda_0\bar{r}) - \lambda_0 J_1(\lambda_0\bar{r})J_0(\lambda_0\bar{r})\right] \cong -\tfrac{1}{4}c^2\lambda_0^2\kappa^2\bar{r}[1-\tfrac{1}{2}\lambda_0^2\bar{r}^2+\tfrac{5}{64}\lambda_0^4\bar{r}^4-\lambda_0^2\bar{z}^2(1-\tfrac{1}{4}\lambda_0^2\bar{r}^2+\tfrac{5}{192}\lambda_0^4\bar{r}^4)] \tag{25}$$

$$\frac{\partial \bar{p}}{\partial \bar{z}} = -c^2\lambda_0^2\kappa^2\bar{z}[J_0^2(\lambda_0\bar{r})+J_1^2(\lambda_0\bar{r})] \cong -c^2\lambda_0^2\kappa^2\bar{z}(1-\tfrac{1}{4}\lambda_0^2\bar{r}^2+\tfrac{1}{32}\lambda_0^4\bar{r}^4-\tfrac{5}{2304}\lambda_0^6\bar{r}^6)+\ldots \tag{26}$$

Using $\bar{p}_0$ to define the normalized pressure at the head-end center, we can write $\Delta\bar{p} = \bar{p}-\bar{p}_0$ and integrate Eqs. (25)-(26) to arrive at

$$\begin{aligned}\Delta\bar{p} &= -\tfrac{1}{2}c^2\kappa^2\{J_1^2(\lambda_0\bar{r})+\lambda_0^2\bar{z}^2[J_0^2(\lambda_0\bar{r})+J_1^2(\lambda_0\bar{r})]\}\\ &\cong -\tfrac{1}{8}c^2\lambda_0^2\kappa^2\left[\bar{r}^2-\tfrac{1}{4}\lambda_0^2\bar{r}^4+\tfrac{5}{192}\lambda_0^4\bar{r}^6+\bar{z}^2(4-\lambda_0^2\bar{r}^2+\tfrac{1}{8}\lambda_0^4\bar{r}^4-\tfrac{5}{576}\lambda_0^6\bar{r}^6)+\ldots\right]\end{aligned} \tag{27}$$

Figure 5a illustrates the radial variation of $\Delta\bar{p}/\kappa^2$ at several axial stations that are evenly distributed along the chamber length. Being referenced to its value at $\bar{z}=0$, the pressure differential varies from a small value at the headwall to $-69.2\kappa^2$ at $\bar{z}=1$. Its prediction differs considerably from the $-\tfrac{1}{2}\bar{r}^{-2}$ behavior shown in Fig. 5b and associated with free vortex motion. The pressure gradients in the radial and axial directions are further shown in Figs. 5c-d. Note that the locus of the peak radial pressure gradient is centralized, ranging between $\bar{r}=0.722183$ and 0.355474 for $0 \le \bar{z} \le 2.92224$. Despite the apparently large pressure gradients, actual magnitudes are reasonably tempered owing to the impending multiplication by κ^2. As we move downstream, the axial pressure gradient changes rapidly along the centerline and gradually along the sidewall. This behavior may be viewed as an improvement over the $\partial\bar{p}/\partial\bar{z} = -4\pi^2\kappa^2\bar{z}$ relation associated with the sinusoidal solution. The latter remains radially invariant while changing linearly with the distance from the headwall. The increased pressure gradient in the core seems to suggest a faster moving core flow which, in turn, could be a performance enhancer.

To capture the two related solutions side-by-side, their streamlines are plotted in Fig. 6 using two chamber aspect ratios. It is interesting to note the strong similarities between the two motions despite the slight shift in their flow turning points. In fact, the two families of streamlines shown in the $\bar{r}-\bar{z}$ plane seem to mirror each other almost identically. The superimposition of swirl causes fluid particles entering the chamber to spin around while scooping down the chamber bore. Their motion is accompanied by uniform mass transport along the (chained) interface that separates the annular downdraft from the tubular updraft. Although not shown, the swirling speed of the returning stream increases with the distance from the headwall because of the angular momentum that it carries inwardly and the merging with the radial mass crossing the mantle. This behavior is corroborated by several reported experiments and numerical simulations including those by Smith,[11-12] Hoekstra, Derksen and Van Den Akker,[18] Anderson *et al.*,[50] and Hu *et al.*[23] The vorticity and swirling intensity carried by the flow can also be examined. The latter may be evaluated directly from[51]

$$\tilde{\Omega} = \tfrac{1}{4}\int_0^\beta \bar{u}_z\bar{u}_\theta\bar{r}\,\mathrm{d}\bar{r}\left(\int_0^\beta \bar{u}_z\bar{r}\,\mathrm{d}\bar{r}\right)^{-2} = \tfrac{1}{24}\beta\lambda_0^3\;{}_2F_3\left[\left(\tfrac{3}{2},\tfrac{3}{2}\right),\left(2,2,\tfrac{5}{2}\right),-\beta^2\lambda_0^2\right]J_1^{-2}\left(\beta\lambda_0\right) \cong 1.34067 \tag{28}$$

The constancy of the swirling intensity stands in sharp contrast to the spatially varying value of $5.443\sigma l/\bar{z}$ that accompanies the sinusoidal solution. Instead of peaking near the headwall or increasing with the swirl number as before, the present model yields a uniformly distributed swirling intensity throughout the chamber volume, regardless of inlet conditions. This could be interpreted as a condition conducive of spatial constancy in mixing efficacy. Graphically, the pitch angle of a spiraling streamline will be uniform in comparison to its complex lamellar counterpart which varies from a small angle at the headwall to a large value over the body of the cylinder.

Another distinguishing attribute may be examined by evaluating the vorticity. This may be readily expressed using $\bar{\boldsymbol{\omega}} = \nabla\times\bar{\boldsymbol{u}}$ or

$$\begin{aligned}\bar{\boldsymbol{\omega}} &= -c\lambda_0\kappa J_1\left(\lambda_0\bar{r}\right)\boldsymbol{e}_r + c\lambda_0^2\kappa\bar{z}J_1\left(\lambda_0\bar{r}\right)\boldsymbol{e}_\theta + c\lambda_0^2\kappa\bar{z}J_0\left(\lambda_0\bar{r}\right)\boldsymbol{e}_z\\ &= -11.7601\kappa J_1\left(\lambda_0\bar{r}\right)\boldsymbol{e}_r + 45.0611\bar{z}J_1\left(\lambda_0\bar{r}\right)\boldsymbol{e}_\theta + 45.0611\bar{z}J_0\left(\lambda_0\bar{r}\right)\boldsymbol{e}_z\end{aligned} \tag{29}$$

In the same vein, the vorticity magnitude may be estimated from

$$\bar{\omega} = c\lambda_0\kappa J_1\left(\lambda_0\bar{r}\right)\sqrt{1+\lambda_0^2\bar{z}^2\left[1+J_0^2\left(\lambda_0\bar{r}\right)/J_1^2\left(\lambda_0\bar{r}\right)\right]} \tag{30}$$

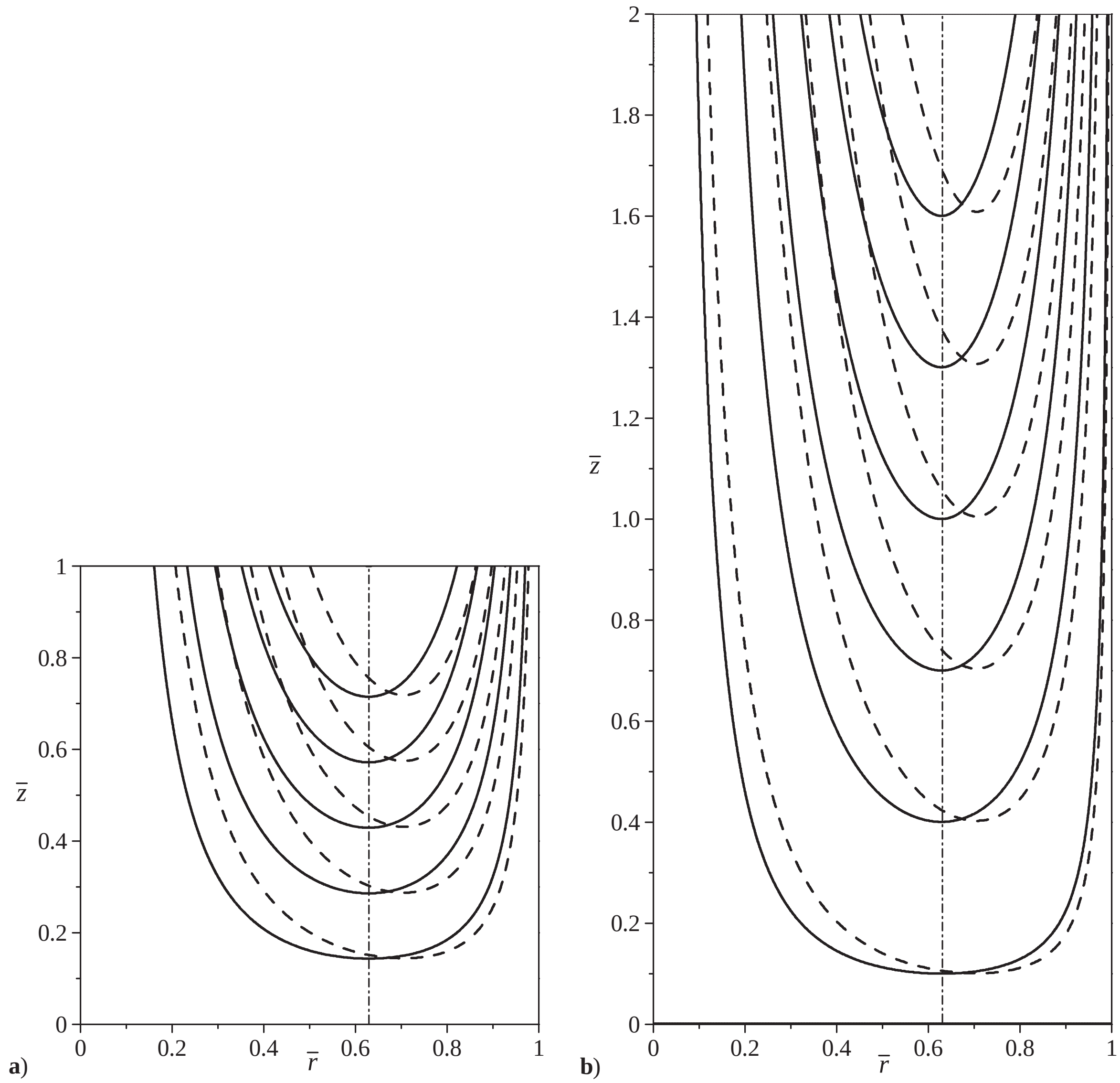

Figure 6. Flow streamlines comparing the present model (solid lines) to the sinusoidal solution (broken lines). Results are shown for two chamber aspect ratios of a) *l* = 1 and b) *l* = 2.

This result is substantially different from the swirl dominated complex lamellar solution which, in hindsight, was somewhat limited in that it could only engender one component of vorticity, namely, $\bar{\omega}_\theta = 4\pi^2\kappa\bar{r}\bar{z}\sin(\pi\bar{r}^2)$. The two additional components of vorticity that arise here stem from the axial dependence of $\bar{u}_\theta$. At first glance, it may be surmised that Eq. (29) bears a striking resemblance to Eq. (21). Upon further scrutiny, however, we find the vorticity to be directly proportional to the velocity through $\bar{\boldsymbol{\omega}} = \lambda_0\bar{\boldsymbol{u}}$. This vector parallelism is accompanied by a vanishing Lamb vector ($\bar{\boldsymbol{\omega}}\times\bar{\boldsymbol{u}} = 0$), a defining characteristic of the Beltramian family of fluid motions in which the main source of nonlinearity is eliminated. The corresponding Helmholtz equation is linearized, thus giving rise to simple exact solutions of swirling motions.[52] Note that the velocity in $\nabla\times\bar{\boldsymbol{u}} = \lambda_0\bar{\boldsymbol{u}}$ plays the role of an eigenvector of the curl operator connected with the eigenvalue λ_0. Within this class of helical fields, our flow is specifically called Trkalian because of the constancy of λ_0.[53] Being a Trkalian profile, it forms a basis vector of helical wave decomposition and may be used to appropriately represent steady, incompressible, and chaotic motions in a frictionless environment.

Figure 7a illustrates the vorticity distribution along the chamber cross section at select axial positions. Except for the region in the immediate vicinity of the headwall, it can be seen that vorticity is amplified near the centerline and continues to grow in the downstream direction. This behavior is corroborated in Fig. 7b where contours of

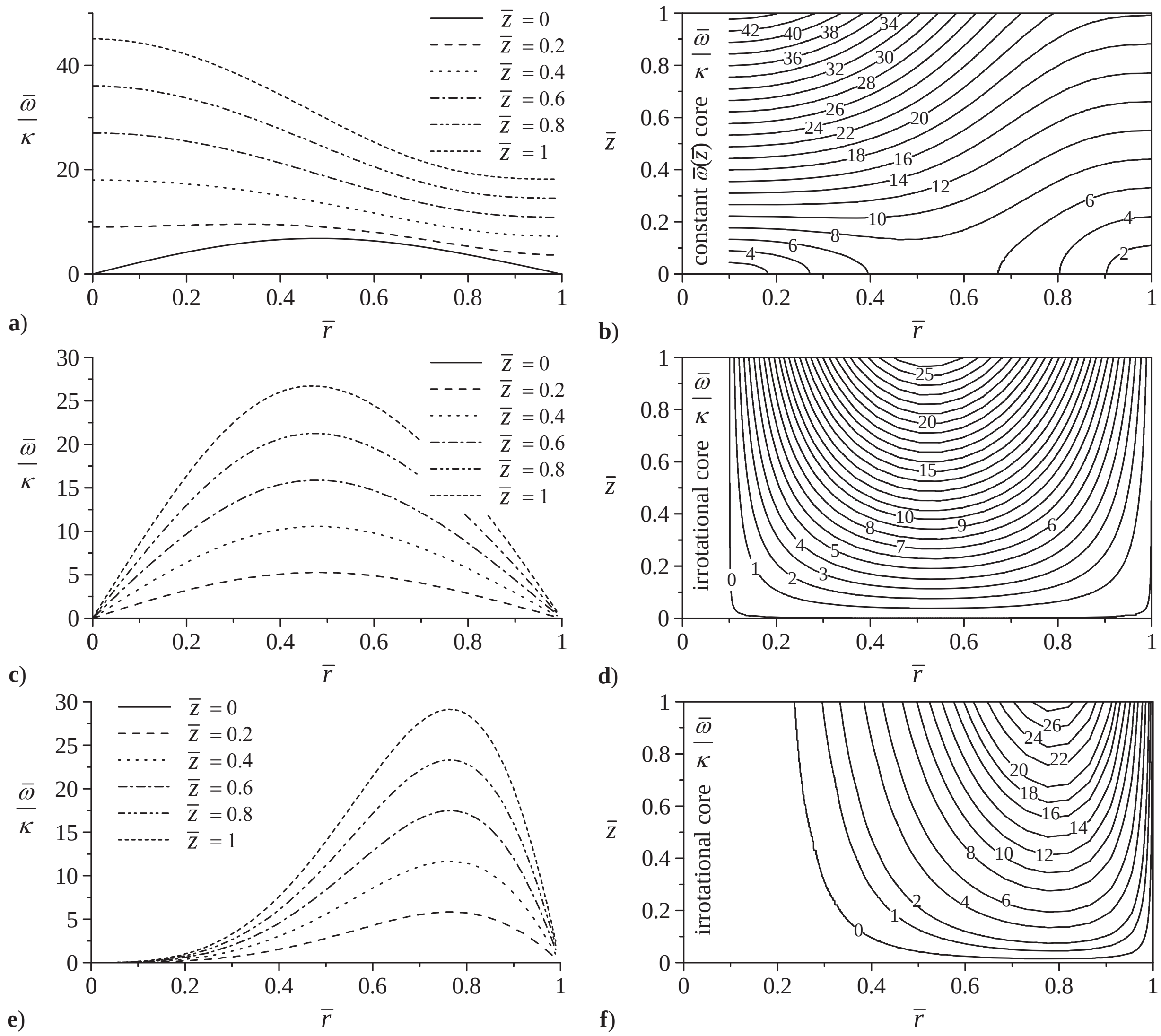

Figure 7. Radial distribution of total vorticity along fixed a) axial positions and b) isolines. The same is repeated in c- d) for the slip permitting solution, and in e-f) for the sinusoidal model by Vyas and Majdalani.[29]

isovorticity are presented in the $\bar{r}-\bar{z}$ plane. In relative proportion to the azimuthal vorticity of its sinusoidal predecessor, the most significant differences arise in the core region and the immediate vicinity of the wall.

C. Solution for a Non-vanishing Circumferential Velocity

In the foregoing analysis, the swirl velocity was made to artificially vanish at the sidewall. However, such a condition is expendable in a frictionless environment. In mirroring the solution developed by Vyas and Majdalani,[29] we put $u_\theta(a,L)=U$ such that $B_1=U^2a^2$ may be retrieved from Eq. (4). This condition only affects the swirl component of the velocity which takes the form:

$$u_\theta=\frac{1}{r}\left[\psi_0^2\lambda_0^2 r^2\left(\frac{z}{a}\right)^2 J_1^2\left(\lambda_0\frac{r}{a}\right)+U^2a^2\right]^{1/2} \tag{31}$$

where Eq. (31) refers to a solution that permits slip at the sidewall and, for similar reasons, becomes infinitely large at the centerline. Suppressing the inherent singularity at $r=0$ will have to be achieved using a suitable boundary layer treatment. Note that $\underline{u}_\theta$ bears a striking resemblance to the form obtained by Barber and Majdalani.[41] It is strongly dominated by the free vortex behavior of its leading order part and displays only weak dependence on the spatially varying stream function. In dimensionless form, Eq. (31) collapses into

$$\bar{u}_\theta = \frac{\bar{\mathrm{B}}}{\bar{r}} = \frac{1}{\bar{r}}\sqrt{1+\lambda_0^2\bar{\psi}^2} = \frac{1}{\bar{r}}\left[1+\frac{\lambda_0^2\kappa^2\bar{r}^2\bar{z}^2J_1^2\left(\lambda_0\bar{r}\right)}{\beta^2J_1^2\left(\lambda_0\beta\right)}\right]^{1/2} = \frac{1}{\bar{r}}\sqrt{1+c^2\lambda_0^2\kappa^2\bar{r}^2\bar{z}^2J_1^2\left(\lambda_0\bar{r}\right)} \tag{32}$$

Before evaluating the induced pressure and vorticity, it may be useful to express the complete solution viz.

$$\bar{\boldsymbol{u}} = -3.069\kappa J_1\left(\lambda_0\bar{r}\right)\boldsymbol{e}_r + \frac{1}{\bar{r}}\left[1+138.3\kappa^2\bar{r}^2\bar{z}^2J_1^2\left(\lambda_0\bar{r}\right)\right]^{1/2}\boldsymbol{e}_\theta + 11.76\kappa\bar{z}J_0\left(\lambda_0\bar{r}\right)\boldsymbol{e}_z \tag{33}$$

We mention in passing that the axisymmetric streamlines associated with Eq. (33) coincide with the solid curves shown in the $\bar{r}-\bar{z}$ plane of Fig. 6. As for the corresponding radial and axial pressure gradients, these may be readily extracted from Euler's momentum equation. We find, in relation to the just computed solution with no slip,

$$\begin{aligned}\frac{\partial\bar{p}}{\partial\bar{r}} = \left(\frac{\partial\bar{p}}{\partial\bar{r}}\right)_{\text{noslip}} + \bar{r}^{-3} &= \frac{1+c^2\kappa^2\bar{r}^2J_1(\lambda_0\bar{r})\left[(1+\lambda_0^2\bar{z}^2)J_1(\lambda_0\bar{r})-\lambda_0\bar{r}J_0(\lambda_0\bar{r})\right]}{\bar{r}^3}\\ &\cong \bar{r}^{-3} - \tfrac{1}{4}c^2\lambda_0^2\kappa^2\bar{r}\left[1-\tfrac{1}{2}\lambda_0^2\bar{r}^2+\tfrac{5}{64}\lambda_0^4\bar{r}^4-\tfrac{7}{1152}\lambda_0^6\bar{r}^6-\lambda_0^2\bar{z}^2(1-\tfrac{1}{4}\lambda_0^2\bar{r}^2+\tfrac{5}{192}\lambda_0^4\bar{r}^4-\tfrac{7}{4608}\lambda_0^6\bar{r}^6)\right]\end{aligned} \tag{34}$$

$$\frac{\partial\bar{p}}{\partial\bar{z}} = \left(\frac{\partial\bar{p}}{\partial\bar{z}}\right)_{\text{noslip}} = -c^2\lambda_0^2\kappa^2\bar{z}[J_0^2(\lambda_0\bar{r})+J_1^2(\lambda_0\bar{r})] \cong -c^2\kappa^2\lambda_0^2\bar{z}(1-\tfrac{1}{4}\lambda_0^2\bar{r}^2+\tfrac{1}{32}\lambda_0^4\bar{r}^4-\tfrac{5}{2304}\lambda_0^6\bar{r}^6)+\ldots \tag{35}$$

Then using $\bar{p}_0$ to define the normalized pressure at the head-end center, partial integration toward the form $\Delta\bar{p} = \bar{p}-\bar{p}_0$ leads to

$$\begin{aligned}\Delta\bar{p} = \left(\Delta\bar{p}\right)_{\text{noslip}} - \tfrac{1}{2}\bar{r}^{-2} &= -\tfrac{1}{2}\bar{r}^{-2} - \tfrac{1}{2}c^2\kappa^2\{J_1^2(\lambda_0\bar{r})+\lambda_0^2\bar{z}^2[J_0^2(\lambda_0\bar{r})+J_1^2(\lambda_0\bar{r})]\}\\ &\cong -\tfrac{1}{2}\bar{r}^{-2} - \tfrac{1}{8}c^2\lambda_0^2\kappa^2\left[\bar{r}^2-\tfrac{1}{4}\lambda_0^2\bar{r}^4+\tfrac{5}{192}\lambda_0^4\bar{r}^6+\bar{z}^2(4-\lambda_0^2\bar{r}^2+\tfrac{1}{8}\lambda_0^4\bar{r}^4-\tfrac{5}{576}\lambda_0^6\bar{r}^6)+\ldots\right]\end{aligned} \tag{36}$$

Unlike Fig. 5a in which the pressure variation remains finite, $\Delta\bar{p}$ is largely dominated by the sharp sloping $-\frac{1}{2}\bar{r}^{-2}$ distribution depicted in Fig. 5b. In the same vein, owing to the free vortex divergence near the axis of rotation, the radial pressure gradient is seen to be controlled by the $\bar{r}^{-3}$ behavior displayed in Fig. 5c. This behavior is identical to that associated with the complex lamellar solution of Vyas and Majdalani.[29] As for the axial pressure gradient, it remains independent of the swirl velocity contribution and is suitably described in Fig. 5d.

Lastly for this case, the mean flow vorticity may be directly evaluated and expressed as

$$\bar{\boldsymbol{\omega}} = -\frac{138.3\kappa^2\bar{r}\bar{z}J_1^2\left(\lambda_0\bar{r}\right)}{\sqrt{1+138.3\kappa^2\bar{r}^2\bar{z}^2J_1^2\left(\lambda_0\bar{r}\right)}}\boldsymbol{e}_r + 45.06\kappa\bar{z}J_1\left(\lambda_0\bar{r}\right)\boldsymbol{e}_\theta + \frac{529.92\kappa^2\bar{r}\bar{z}^2J_0\left(\lambda_0\bar{r}\right)J_1\left(\lambda_0\bar{r}\right)}{\sqrt{1+138.3\kappa^2\bar{r}^2\bar{z}^2J_1^2\left(\lambda_0\bar{r}\right)}}\boldsymbol{e}_z \tag{37}$$

As it may be expected, the spatial distribution of vorticity is dominated by its tangential component $\bar{\omega}_\theta$. This, in turn, mirrors the tangential velocity given by Eq. (21) except for its magnitude being 3.832 larger. Forthwith, the radial distribution of $\bar{\omega}/\kappa$ is illustrated in Fig. 7c at several axial stations. It is clear that the vorticity vanishes at the headwall, sidewall, and centerline, where an irrotational vortex is established. The onset of an irrotational core about the $z-$axis is further corroborated by the contour plots of isovorticity rendered in Fig. 7d. These confirm that vorticity increases in the positive downstream direction and reaches its peak value at $\bar{r}_{\max} = 0.480513$. In fact, the maximum vorticity at any axial station may be readily calculated from

$$\bar{\omega}_{\max} = 26.22\kappa\bar{z}\left[1+2.1749\kappa^2(0.338567+6.43717\bar{z}^2)\right]^{\frac{1}{2}} / \left(1+10.811\kappa^2\bar{z}^2\right)^{\frac{1}{2}} \geq 26.22\kappa\bar{z} \tag{38}$$

It may be instructive to note that, despite its inclusion of an irrotational core, the vorticity distribution associated with Eq. (37) is spread over a relatively wide chamber interval. This is especially true when compared to the vorticity generated by the complex lamellar profile of Vyas and Majdalani.[29] The latter is described in Figs. 7e-f where a major vorticity concentration is located away from the centerline, thus leading to a substantially wider irrotational core region. By comparing the various contours in Fig. 7, it appears that the solutions discussed above exhibit from top to bottom, increasingly wider irrotational segments. While Eq. (31) corresponds to a Beltramian flow for which $\bar{\boldsymbol{\omega}}\times\bar{\boldsymbol{u}} = 0$, it remains non-Trkalian because of its spatially varying ratio of vorticity and velocity, namely,

$$\frac{\bar{\boldsymbol{\omega}}}{\bar{\boldsymbol{u}}} = \lambda_0\left[1+\frac{1}{c^2\kappa^2\lambda_0^2\bar{r}^2\bar{z}^2J_1^2\left(\lambda_0\bar{r}\right)}\right]^{-1/2} \tag{39}$$

For the reader's convenience, the principal equations associated with the $\upsilon = 0$ case are catalogued in Table 3.

Table 3. Cases of $\upsilon = 0$

Variable	Equation
	<u>Common parts</u>
$\bar{\psi}$	$c\kappa\bar{z}\,\bar{r}J_1(\lambda_0\bar{r})$
$(\bar{u}_r)_{\mathrm{cross}}$	-1.5933κ
$(\bar{u}_r)_{\max}$	-1.7858κ
$\dfrac{\partial\bar{p}}{\partial\bar{z}}$	$-c^2\lambda_0^2\kappa^2\bar{z}[J_0^2(\lambda_0\bar{r})+J_1^2(\lambda_0\bar{r})]$
	<u>Case with no slip</u>
$\bar{\boldsymbol{u}}$	$-c\kappa J_1(\lambda_0\bar{r})\boldsymbol{e}_r + c\lambda_0\kappa\bar{z}J_1(\lambda_0\bar{r})\boldsymbol{e}_\theta + c\lambda_0\kappa\bar{z}J_0(\lambda_0\bar{r})\boldsymbol{e}_z$
$\bar{\boldsymbol{\omega}}$	$-c\lambda_0\kappa J_1(\lambda_0\bar{r})\boldsymbol{e}_r + c\lambda_0^2\kappa\bar{z}J_1(\lambda_0\bar{r})\boldsymbol{e}_\theta + c\lambda_0^2\kappa\bar{z}J_0(\lambda_0\bar{r})\boldsymbol{e}_z$
$(\bar{u}_\theta)_{\max}$	$6.8428\kappa\bar{z}$
$\dfrac{\partial\bar{p}}{\partial\bar{r}}$	$c^2\kappa^2\left[\dfrac{(1+\lambda_0^2\bar{z}^2)}{\bar{r}}J_1^2(\lambda_0\bar{r})-\lambda_0 J_1(\lambda_0\bar{r})J_0(\lambda_0\bar{r})\right]$
$\Delta\bar{p}$	$-\frac{1}{2}c^2\kappa^2\{J_1^2(\lambda_0\bar{r})+\lambda_0^2\bar{z}^2[J_0^2(\lambda_0\bar{r})+J_1^2(\lambda_0\bar{r})]\}$
$\tilde{\Omega}$	$\frac{1}{24}\beta\lambda_0^3\,{}_2F_3\left[\left(\frac{3}{2},\frac{3}{2}\right),\left(2,2,\frac{5}{2}\right),-\beta^2\lambda_0^2\right]J_1^{-2}(\beta\lambda_0)\cong 1.34067$
	<u>Case with slip</u>
$\bar{\boldsymbol{u}}$	$-c\kappa J_1(\lambda_0\bar{r})\boldsymbol{e}_r + \dfrac{1}{\bar{r}}\sqrt{1+c^2\lambda_0^2\kappa^2\bar{r}^2\bar{z}^2J_1^2(\lambda_0\bar{r})}\,\boldsymbol{e}_\theta + c\lambda_0\kappa\bar{z}J_0(\lambda_0\bar{r})\boldsymbol{e}_z$
$\bar{\boldsymbol{\omega}}$	$-\dfrac{c^2\lambda_0^2\kappa^2\bar{r}\bar{z}J_1^2(\lambda_0\bar{r})}{\sqrt{1+c^2\lambda_0^2\kappa^2\bar{r}^2\bar{z}^2J_1^2(\lambda_0\bar{r})}}\boldsymbol{e}_r + c\lambda_0^2\kappa\bar{z}J_1(\lambda_0\bar{r})\boldsymbol{e}_\theta + \dfrac{c^2\lambda_0^3\kappa^2\bar{r}\bar{z}^2J_0(\lambda_0\bar{r})J_1(\lambda_0\bar{r})}{\sqrt{1+c^2\lambda_0^2\kappa^2\bar{r}^2\bar{z}^2J_1^2(\lambda_0\bar{r})}}\boldsymbol{e}_z$
$(\bar{u}_\theta)_{\max}$	∞
$\dfrac{\partial\bar{p}}{\partial\bar{r}}$	$\dfrac{1}{\bar{r}^3}+c^2\kappa^2\left[\dfrac{(1+\lambda_0^2\bar{z}^2)}{\bar{r}}J_1^2(\lambda_0\bar{r})-\lambda_0 J_1(\lambda_0\bar{r})J_0(\lambda_0\bar{r})\right]$
$\Delta\bar{p}$	$-\frac{1}{2}\bar{r}^{-2}-\frac{1}{2}c^2\kappa^2\{J_1^2(\lambda_0\bar{r})+\lambda_0^2\bar{z}^2[J_0^2(\lambda_0\bar{r})+J_1^2(\lambda_0\bar{r})]\}$

IV. Other Similarity Conforming Solutions

Pursuant to Eq. (8), two additional forms of solution may be worthwhile to investigate although they are less likely to arise in the context of cyclonic motion. These are

$$\psi(r,z)=\begin{cases}\psi_0 r\sin(\upsilon z)J_1(r\sqrt{C_n^2-\upsilon^2}); & C_n^2>\upsilon^2\\ \psi_0 r\sinh(\upsilon z)J_1(r\sqrt{C_n^2+\upsilon^2}) & \end{cases}\tag{40}$$

where we have set $C_2=0$ and $C_4=0$ to satisfy $u_z(r,0)=0$ and $u_r(0,z)=0$ in Eq. (9), respectively. We have also put $\psi_0\equiv C_1C_3$ with no loss of generality. The third boundary condition left to be applied consists of $u_r(a,z)=0$. This implies:

$$\frac{\partial\psi(a,z)}{\partial z}=\begin{cases}\psi_0 a\upsilon\cos(\upsilon z)J_1(a\sqrt{C_n^2-\upsilon^2})=0\\ \psi_0 a\upsilon\cosh(\upsilon z)J_1(a\sqrt{C_n^2+\upsilon^2})=0\end{cases}\tag{41}$$

These constraints will be satisfied, $\forall z$, when

$$\begin{cases}J_1(a\sqrt{C_n^2-\upsilon^2})=0\\ J_1(a\sqrt{C_n^2+\upsilon^2})=0\end{cases}\quad\begin{cases}\sqrt{C_n^2-\upsilon^2}=\lambda_n/a\\ \sqrt{C_n^2+\upsilon^2}=\lambda_n/a\end{cases}\quad\text{or}\quad\begin{cases}C_n^2=\lambda_n^2/a^2+\upsilon^2\\ C_n^2=\lambda_n^2/a^2-\upsilon^2\end{cases}\tag{42}$$

Here $n \in \mathbb{N}$ and $\lambda_n = (3.83171, 7.01559, ...)$ denote, as before, the roots of the Bessel function of the first kind. For a single head-end reversal, one takes $\lambda_0 = 3.83171$, and so, for the harmonic axial variation, deduce $C_0 = (\lambda_0^2 / a^2 + \upsilon^2)^{1/2}$. The separation constant υ may be determined by imposing an additional physical constraint, such as $u_r(r, L) = 0$. This condition forces the radial velocity to vanish at the endwall where the modeled flow is purely tangential. At the outset, one collects, for the trigonometric approximation,

$$\cos(\upsilon_j L) = 0 \qquad \text{or} \qquad \upsilon_j = (j + \tfrac{1}{2})\pi / L, \quad j \in \mathbb{N} \tag{43}$$

To prevent the formation of undesirable recirculatory flows in the axial direction, we limit our attention to $\upsilon = \upsilon_0 = \frac{1}{2}\pi / L$. We recognize that other forms exist but these may find applications in physical settings that fall outside the scope of this investigation. For the hypergeometric function representation, no plausible condition may be accommodated for the problem at hand. For this reason, its analysis is relegated to later study. In what follows, we focus our attention on

$$\psi(r,z) = \psi_0 r \sin(\tfrac{1}{2}\pi z / L) J_1(\lambda_0 r / a); \quad C_0 = \sqrt{\lambda_0^2 / a^2 + \tfrac{1}{4}\pi^2 / L^2}. \tag{44}$$

The solution at this point may be expressed as

$$\boldsymbol{u} = -\frac{\pi\psi_0}{2L}\cos\left(\frac{\pi z}{2L}\right) J_1\left(\lambda_0 \frac{r}{a}\right)\boldsymbol{e}_r + \frac{1}{r}\sqrt{\psi_0^2 r^2\left(\frac{\lambda_0^2}{a^2} + \frac{\pi^2}{4L^2}\right)\sin^2\left(\frac{\pi z}{2L}\right) J_1^2\left(\lambda_0 \frac{r}{a}\right) + B_1}\,\boldsymbol{e}_\theta + \frac{\psi_0}{a}\lambda_0 \sin\left(\frac{\pi z}{2L}\right) J_0\left(\lambda_0 \frac{r}{a}\right)\boldsymbol{e}_z \tag{45}$$

where ψ_0 may be obtained from global mass conservation. One gets

$$\psi_0 = Q_i \left[2\pi a \beta J_1(\lambda_0 \beta)\right]^{-1} \tag{46}$$

Concerning the last remaining constant, B_1, it will be either nil or $U^2 a^2$ depending on whether we set $u_\theta(a,z) = 0$, or U, respectively.

A. Axially Harmonic Solution with No Slip

The solution becomes, for the motion compelled to satisfy no slip at $r = a$,

$$\begin{cases} \psi = \dfrac{Q_i}{2\pi a \beta J_1(\lambda_0\beta)} r \sin\left(\dfrac{\pi z}{2L}\right) J_1\left(\lambda_0 \dfrac{r}{a}\right) \\ u_r = -\dfrac{\pi Q_i}{4\pi a L \beta J_1(\lambda_0\beta)} \cos\left(\dfrac{\pi z}{2L}\right) J_1\left(\lambda_0 \dfrac{r}{a}\right) \\ u_\theta = \dfrac{Q_i}{2\pi a \beta J_1(\lambda_0\beta)} \sqrt{\dfrac{\lambda_0^2}{a^2} + \dfrac{\pi^2}{4L^2}} \sin\left(\dfrac{\pi z}{2L}\right) J_1\left(\lambda_0 \dfrac{r}{a}\right) \\ u_z = \dfrac{Q_i}{2\pi a^2 \beta J_1(\lambda_0\beta)} \lambda_0 \sin\left(\dfrac{\pi z}{2L}\right) J_0\left(\lambda_0 \dfrac{r}{a}\right) \end{cases} \qquad \begin{cases} \bar{\psi} = \dfrac{\kappa l}{\beta J_1(\lambda_0\beta)} \bar{r} \sin\left(\dfrac{\pi \bar{z}}{2l}\right) J_1(\lambda_0 \bar{r}) \\ \bar{u}_r = -\dfrac{\pi}{2}\dfrac{\kappa}{\beta J_1(\lambda_0\beta)} \cos\left(\dfrac{\pi \bar{z}}{2l}\right) J_1(\lambda_0 \bar{r}) \\ \bar{u}_\theta = \dfrac{\kappa}{\beta J_1(\lambda_0\beta)} \sqrt{\lambda_0^2 l^2 + \tfrac{1}{4}\pi^2} \sin\left(\dfrac{\pi \bar{z}}{2l}\right) J_1(\lambda_0 \bar{r}) \\ \bar{u}_z = \dfrac{\kappa l}{\beta J_1(\lambda_0\beta)} \lambda_0 \sin\left(\dfrac{\pi \bar{z}}{2l}\right) J_0(\lambda_0 \bar{r}) \end{cases} \tag{47}$$

For the slip permitting solution, the profile will share the same components except for

$$u_\theta = \frac{1}{r}\sqrt{\left[\frac{Q_i}{2\pi a \beta J_1(\lambda_0\beta)}\right]^2 r^2 \left(\frac{\lambda_0^2}{a^2} + \frac{\pi^2}{4L^2}\right)\sin^2\left(\frac{\pi z}{2L}\right) J_1^2\left(\lambda_0 \frac{r}{a}\right) + U^2 a^2} \tag{48}$$

or, in dimensionless form,

$$\bar{u}_\theta = \frac{1}{\bar{r}}\sqrt{\frac{\kappa^2}{\beta^2 J_1^2(\lambda_0\beta)}\left(\lambda_0^2 l^2 + \tfrac{1}{4}\pi^2\right)\bar{r}^2 \sin^2\left(\frac{\pi \bar{z}}{2l}\right) J_1^2(\lambda_0 \bar{r}) + 1} \tag{49}$$

These two models share the same stream function which is plotted in Fig. 8. In compact notation, we therefore have $\bar{\psi} = c\kappa l \bar{r} \sin\left(\frac{1}{2}\pi \bar{z} / l\right) J_1(\lambda_0 \bar{r})$, and, starting with the velocity adhering solution, $\bar{\mathrm{B}} = [\lambda_0^2 + \frac{1}{4}\pi^2 / l^2]^{1/2}\bar{\psi}$ so that

$$\bar{\boldsymbol{u}} = \begin{cases} -\frac{1}{2}\pi c\kappa \cos\left(\frac{1}{2}\pi\bar{z}/l\right) J_1(\lambda_0\bar{r})\boldsymbol{e}_r + \frac{1}{2}\pi c\kappa\sqrt{1 + 4\lambda_0^2 l^2/\pi^2}\sin\left(\frac{1}{2}\pi\bar{z}/l\right) J_1(\lambda_0\bar{r})\boldsymbol{e}_\theta + c\lambda_0\kappa l \sin\left(\frac{1}{2}\pi\bar{z}/l\right) J_0(\lambda_0\bar{r})\boldsymbol{e}_z \\ -4.821\kappa\cos\left(\frac{1}{2}\pi\bar{z}/l\right) J_1(\lambda_0\bar{r})\boldsymbol{e}_r + 4.821\sqrt{1 + 5.95 l^2}\,\kappa\sin\left(\frac{1}{2}\pi\bar{z}/l\right) J_1(\lambda_0\bar{r})\boldsymbol{e}_\theta + 11.76\kappa l \sin\left(\frac{1}{2}\pi\bar{z}/l\right) J_0(\lambda_0\bar{r})\boldsymbol{e}_z \end{cases} \tag{50}$$

The mantle here remains fixed at 0.6276. Moreover, if we were to evaluate the axial velocity at the endwall, where $\bar{z} = l$, we recover $11.76\kappa l J_0(\lambda_0 \bar{r})$. This local radial distribution is identical to that retrieved from Eq. (21) and

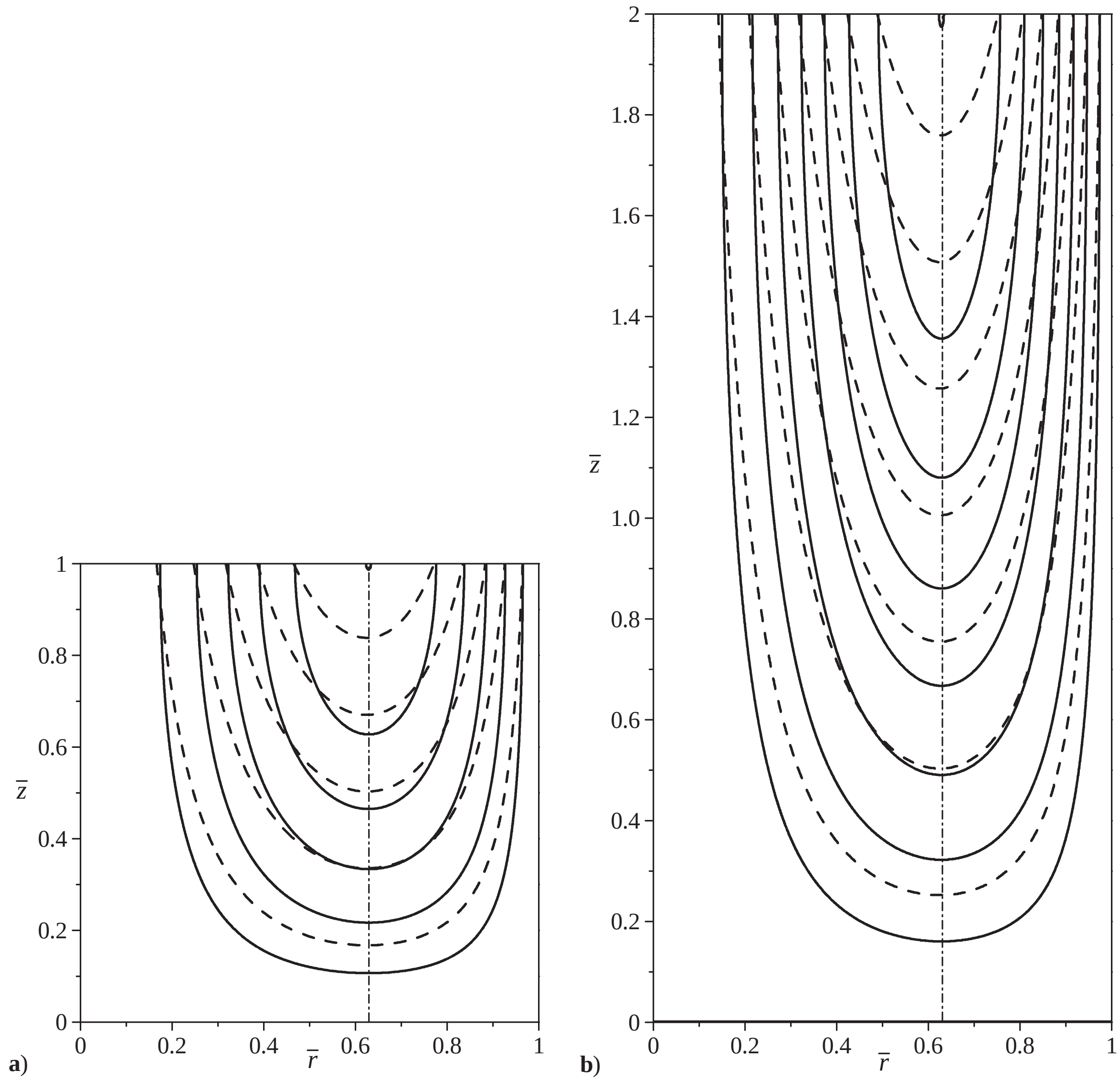

Figure 8. Streamlines for $\upsilon = \frac{1}{2}\pi / L$ (solid lines) and $\upsilon = 0$ (broken lines) using a) l = 1 and b) l = 2.

displayed in Fig. 4a. In contrast, the radial velocity vanishes at the endwall and peaks at the headwall with a value of $-4.821\kappa J_1\left(\lambda_0 \bar{r}\right)$. This outcome corresponds to 1.57 times its counterpart, $-3.069\kappa J_1\left(\lambda_0 \bar{r}\right)$, given by Eq. (21) (and shown in Fig. 4b). These medians given at $\bar{z} = \frac{1}{2} l$ reproduce $\bar{u}_z = 8.32\kappa l J_0\left(\lambda_0 \bar{r}\right)$ and $\bar{u}_r = -3.41\kappa J_1\left(\lambda_0 \bar{r}\right)$, which, in turn, exceed their counterparts in Eq. (21). We infer that both axial and radial velocities associated with this motion tend to exhibit larger magnitudes than those with $\upsilon = 0$, although they remain self-similar in the radial direction. This behavior is clearly illustrated in Fig. 9 where the three velocity components are displayed. The overestimation of the axial and radial velocities predicted by this model constitutes its chief weakness, unless reconciliation with experimental or numerical data may be achieved. The models described heretofore already seem to overpredict available observations and in-house simulations. It is hoped that viscous corrections could be incorporated to help achieve better agreement with physically observed behavior.

From Eq. (50), the radial crossflow velocity along the mantle may be calculated to be

$$(\bar{u}_r)_{\text{cross}} = -2.5028\kappa \cos\left(\tfrac{1}{2}\pi \bar{z} / l\right) \tag{51}$$

Pursuant to this model, the mass transfer across the mantle starts from zero at the endwall and increases to a maximum value of $\left[(\bar{u}_r)_{\text{cross}}\right]_{\max} = -2.5028\kappa$ at the headwall. In particular, given that $2(2.5028)\beta / \pi = 1$, one can verify that

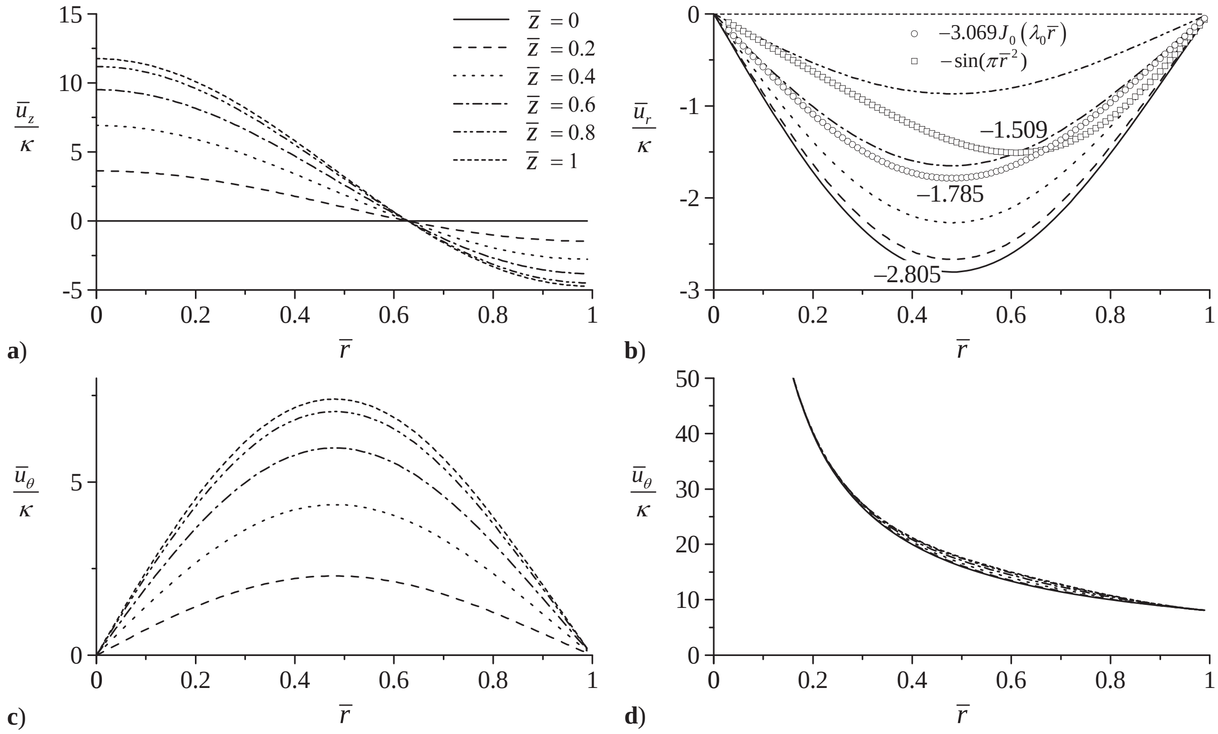

Figure 9. Comparisons for a) axial, b) radial, and c-d) tangential velocity distributions based on the c) slip resistant and d) slip permitting solutions. When needed, we use κ = 0.125 and l =1.

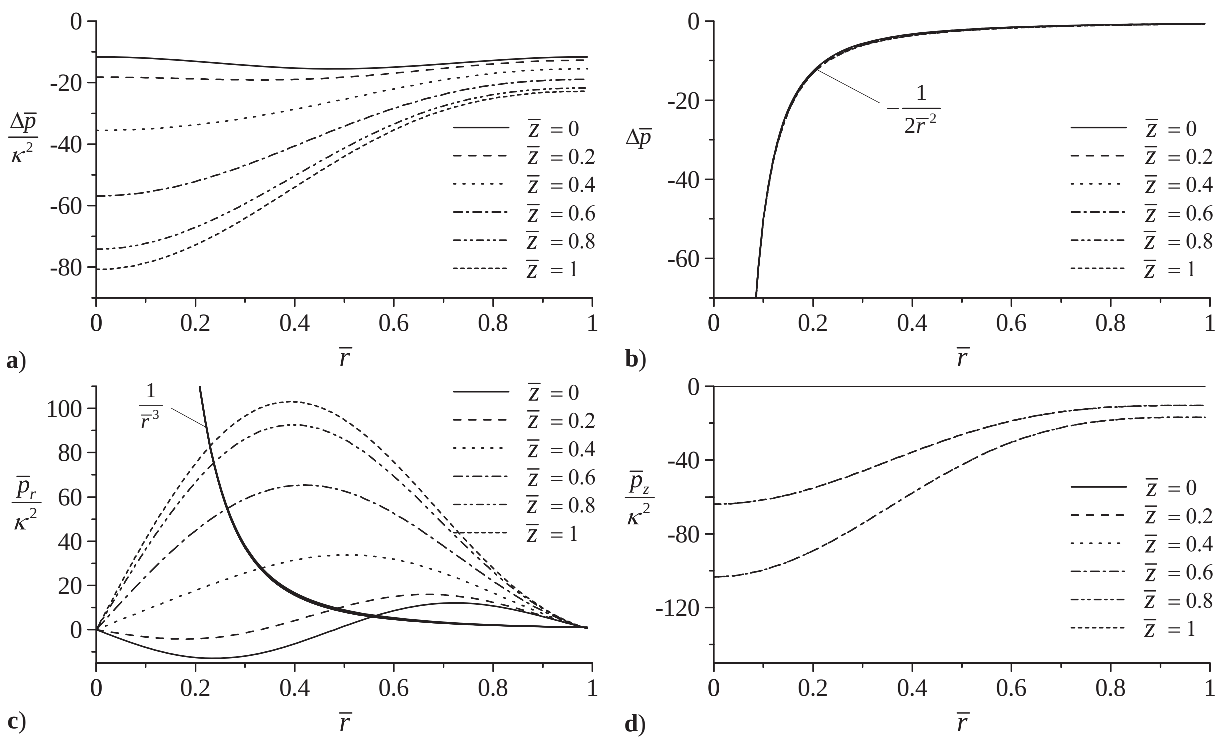

Figure 10. Pressure differential for a) slip resistant and b) slip permitting cases. Corresponding radial and axial pressure gradients are shown in c-d) at several axial positions. Both solutions share the same axial pressure gradient. When needed, we use κ = 0.125 and l =1.

$$2\pi\beta\int_0^l \left|(\bar{u}_r)_{\text{cross}}\right| \mathrm{d}\bar{z} = \sigma^{-1} = \bar{Q}_i \tag{52}$$

In some propulsion-related applications, such as the vortex-fired engine class, this particular variation is advantageous as it suggests a gradual increase in the inward spillage rate, namely, from the outer vortex into the inner vortex. If such a motion could be established in the VCCWC prototype, it would lead to a substantial reduction in early oxidizer leakage, a transport mechanism that ordinarily takes place immediately after injection. As for the maximum radial velocity, it occurs at the same position defined by $\bar{r}_{\max} = 0.4805$. Its calculation leads to:

$$(\bar{u}_r)_{\max} = -2.8052\kappa\cos\left(\tfrac{1}{2}\pi\bar{z}/l\right) \tag{53}$$

which also varies along the length of the chamber. The same may be said of the swirl velocity which peaks at $\bar{r}_{\max}$ with a value of

$$(\bar{u}_\theta)_{\max} = 2.8052\sqrt{1+5.9504l^2}\,\kappa\sin\left(\tfrac{1}{2}\pi\bar{z}/l\right) = 0.4465\sigma^{-1}\sqrt{l^{-2}+5.9504}\sin\left(\tfrac{1}{2}\pi\bar{z}/l\right) \tag{54}$$

Through Eq. (54) it can be seen that $(\bar{u}_\theta)_{\max}$ will peak at entry and vanish at the headwall. While increasing the aspect ratio seems to have a secondary effect on the maximum swirl speed, it appears illogical for $(\bar{u}_\theta)_{\max}$ to be inversely proportional to the swirl number. Such a relation may be attributed to the boundary condition that artificially impedes the tangential velocity at the sidewall.

In mirroring the analysis of Sec. II, the pressure associated with this model can be determined from

$$\frac{\partial\bar{p}}{\partial\bar{r}} = \tfrac{1}{4}c^2\kappa^2 J_1(\lambda_0\bar{r})\left\{-\pi^2\lambda_0 J_0(\lambda_0\bar{r}) + \bar{r}^{-1}J_1(\lambda_0\bar{r})\left[\pi^2 + 2l^2\lambda_0^2 - 2l^2\lambda_0^2\cos\left(\pi\bar{z}/l\right)\right]\right\} \tag{55}$$

$$\frac{\partial\bar{p}}{\partial\bar{z}} = -\tfrac{1}{4}\pi c^2\lambda_0^2\kappa^2 l[J_0^2(\lambda_0\bar{r}) + J_1^2(\lambda_0\bar{r})]\sin\left(\pi\bar{z}/l\right) \tag{56}$$

and so

$$\Delta\bar{p} = -\tfrac{1}{8}c^2\kappa^2\left\{\pi^2\left[1+J_1^2(\lambda_0\bar{r})\right] + 2\lambda_0^2 l^2[J_0^2(\lambda_0\bar{r}) + J_1^2(\lambda_0\bar{r})]\left[1-\cos\left(\pi\bar{z}/l\right)\right]\right\} \tag{57}$$

These expressions are evaluated and plotted in Fig. 10 where they appear to bear strong commonalities with the results of Fig. 5. Compared to the $\upsilon = 0$ solution, we find the pressure excursion and its gradients to be slightly higher in this case, which is consistent with the accompanying increase in velocity magnitudes. The axial pressure gradient is particularly interesting due to its periodicity in $\bar{z}$. This is illustrated in Fig. 10d where the curves corresponding to the (0,1), (0.2,0.8), and (0.5,0.6) pairs of axial positions collapse into three individual lines that share identical values.

The swirling intensity may also be evaluated for the $\upsilon \neq 0$ case. One gets

$$\tilde{\Omega} = \frac{\beta\lambda_0^2\sqrt{\pi^2+4l^2\lambda_0^2}\;{}_2F_3\left[\left(\tfrac{3}{2},\tfrac{3}{2}\right),\left(2,2,\tfrac{5}{2}\right),-\beta^2\lambda_0^2\right]}{48lJ_1^2\left(\beta\lambda_0\right)} \cong 0.549604\sqrt{1+5.9504l^2} \tag{58}$$

It is interesting that $\tilde{\Omega}$ intensifies in elongated chambers for which the length-to-diameter aspect ratio is increased. Turning our attention to the vorticity distribution, we extract

$$\begin{aligned}\bar{\boldsymbol{\omega}} = &-\tfrac{1}{2}c\pi\kappa\sqrt{\lambda_0^2+\tfrac{1}{4}\pi^2/l^2}\,J_1\left(\lambda_0\bar{r}\right)\cos\left(\tfrac{1}{2}\pi\bar{z}/l\right)\boldsymbol{e}_r + c\kappa l(\lambda_0^2+\tfrac{1}{4}\pi^2/l^2)J_1\left(\lambda_0\bar{r}\right)\sin\left(\tfrac{1}{2}\pi\bar{z}/l\right)\boldsymbol{e}_\theta\\ &+c\kappa l\lambda_0\sqrt{\lambda_0^2+\tfrac{1}{4}\pi^2/l^2}\,J_0\left(\lambda_0\bar{r}\right)\sin\left(\tfrac{1}{2}\pi\bar{z}/l\right)\boldsymbol{e}_z\end{aligned} \tag{59}$$

and so

$$\begin{aligned}\bar{\boldsymbol{\omega}} = &-18.473\sqrt{1+0.16806l^{-2}}\,\kappa J_1\left(\lambda_0\bar{r}\right)\cos\left(\tfrac{1}{2}\pi\bar{z}/l\right)\boldsymbol{e}_r + 45.06l\left(1+0.16806l^{-2}\right)\kappa J_1\left(\lambda_0\bar{r}\right)\sin\left(\tfrac{1}{2}\pi\bar{z}/l\right)\boldsymbol{e}_\theta\\ &+18.47268\sqrt{1+5.9504l^2}\,\kappa J_0\left(\lambda_0\bar{r}\right)\sin\left(\tfrac{1}{2}\pi\bar{z}/l\right)\boldsymbol{e}_z\end{aligned} \tag{60}$$

Here too, based on Eqs. (50) and (60), it may be straightforwardly shown that this flow is Trkalian with a configuration specific constant $\bar{\boldsymbol{\omega}}/\bar{\boldsymbol{u}} = \lambda_0[1+\pi^2/(4\lambda_0^2 l^2)]^{1/2}$. This vorticity-to-velocity ratio remains globally fixed for a given chamber aspect ratio l.

B. Axially Harmonic Solution with Slip

As we move to consider the slip-permitting solution, we note that only the swirl velocity distribution becomes affected by the normalized $\bar{u}_\theta(1,z) = 1$ constraint and, by association, the vorticity, radial pressure gradient, and total pressure drop. The axial pressure gradient remains unaffected as it contains no contributions from $\bar{u}_\theta$. The dimensionless angular momentum reduces to $\bar{\mathrm{B}} = [1+(\lambda_0^2+\tfrac{1}{4}\pi^2/l^2)\bar{\psi}^2]^{1/2}$. This enables us to write

$$\bar{u}_\theta = \frac{1}{\bar{r}}\sqrt{1+c^2\kappa^2\left(\lambda_0^2 l^2+\tfrac{1}{4}\pi^2\right)\bar{r}^2 J_1^2\left(\lambda_0\bar{r}\right)\sin^2\left(\frac{\pi\bar{z}}{2l}\right)} = \frac{1}{\bar{r}}\sqrt{1+23.242(1+5.9504l^2)\kappa^2\bar{r}^2 J_1^2\left(\lambda_0\bar{r}\right)\sin^2\left(\frac{\pi\bar{z}}{2l}\right)} \quad (61)$$

which coincides with Eq. (49). While the crossflow and maximum radial speeds remain unchanged, the maximum swirl speed becomes unbounded in the absence of viscous damping (Fig. 9d). For the same reason, a core singularity emerges in the radial pressure gradient that is analogous to that of Eq. (34). This can be seen in

$$\begin{aligned}\frac{\partial\bar{p}}{\partial\bar{r}} &= \left(\frac{\partial\bar{p}}{\partial\bar{r}}\right)_{\text{noslip}} + \frac{1}{\bar{r}^3} = \bar{r}^{-3} + \tfrac{1}{4}c^2\kappa^2 J_1(\lambda_0\bar{r})\left\{-\pi^2\lambda_0 J_0(\lambda_0\bar{r}) + \bar{r}^{-1}J_1(\lambda_0\bar{r})\left[\pi^2+2l^2\lambda_0^2-2l^2\lambda_0^2\cos\left(\pi\bar{z}/l\right)\right]\right\}\\ &\cong \bar{r}^{-3} - \tfrac{1}{16}\pi^2 c^2\lambda_0^2\kappa^2\bar{r}\left[1-\lambda_0^2\left(2\pi^{-2}l^2+\tfrac{1}{2}\bar{r}^2\right)+\tfrac{1}{2}\pi^{-2}\lambda_0^4 l^2\bar{r}^2 + 2\pi^{-2}\lambda_0^2 l^2\left(1-\tfrac{1}{4}\lambda_0^2\bar{r}^2\right)\cos\left(\pi\bar{z}/l\right)+\ldots\right]\end{aligned} \quad (62)$$

$$\begin{aligned}\frac{\partial\bar{p}}{\partial\bar{r}} = \left(\frac{\partial\bar{p}}{\partial\bar{z}}\right)_{\text{noslip}} &= -\tfrac{1}{4}\pi c^2\lambda_0^2\kappa^2 l[J_0^2(\lambda_0\bar{r})+J_1^2(\lambda_0\bar{r})]\sin\left(\pi\bar{z}/l\right)\\ &\cong -\tfrac{1}{4}\pi c^2\lambda_0^2\kappa^2 l\left(1-\tfrac{1}{4}\bar{r}^2\lambda_0^2+\tfrac{1}{32}\bar{r}^4\lambda_0^4\right)\sin\left(\pi\bar{z}/l\right)+\ldots\end{aligned} \quad (63)$$

$$\begin{aligned}\Delta\bar{p} &= \left(\Delta\bar{p}\right)_{\text{noslip}} - \tfrac{1}{2}\bar{r}^{-2} = -\tfrac{1}{2}\bar{r}^{-2} - \tfrac{1}{8}c^2\kappa^2\left\{\pi^2\left[1+J_1^2(\lambda_0\bar{r})\right]+2\lambda_0^2 l^2[J_0^2(\lambda_0\bar{r})+J_1^2(\lambda_0\bar{r})]\left[1-\cos\left(\pi\bar{z}/l\right)\right]\right\}\\ &\cong -\tfrac{1}{2}\bar{r}^{-2} - \tfrac{1}{8}c^2\kappa^2\left[\begin{aligned}&\pi^2+2\lambda_0^2 l^2+\tfrac{1}{4}\pi^2\lambda_0^2\bar{r}^2-\tfrac{1}{2}\lambda_0^4 l^2\bar{r}^2-\tfrac{1}{16}\pi^2\lambda_0^4\bar{r}^4\\ &+\tfrac{1}{16}\lambda_0^6 l^2\bar{r}^4-2\lambda_0^2 l^2\left(1-\tfrac{1}{4}\lambda_0^2\bar{r}^2+\tfrac{1}{32}\lambda_0^4\bar{r}^4\right)\cos\left(\pi\bar{z}/l\right)+\ldots\end{aligned}\right]\end{aligned} \quad (64)$$

where the recurring $\bar{r}^{-3}$ and $-\frac{1}{2}\bar{r}^{-2}$ terms that arise in the radial pressure gradient and pressure drop are characteristic of free vortex behavior. They coincide with their predecessors obtained by Vyas and Majdalani.[29]

Finally, the vorticity for this profile begets

$$\begin{aligned}\bar{\boldsymbol{\omega}} = &-\frac{36.509(1+5.9504l^2)\kappa^2\bar{r}J_1^2\left(\lambda_0\bar{r}\right)\sin\left(\pi\bar{z}/l\right)}{l\sqrt{4+92.968(1+5.9504l^2)\kappa^2\bar{r}^2J_1^2\left(\lambda_0\bar{r}\right)\sin^2\left(\frac{1}{2}\pi\bar{z}/l\right)}}\boldsymbol{e}_r + \frac{7.5728(1+5.9504l^2)}{l}\kappa J_1\left(\lambda_0\bar{r}\right)\sin\left(\tfrac{1}{2}\pi\bar{z}/l\right)\boldsymbol{e}_\theta\\ &+\frac{89.057(1+5.9504l^2)\kappa^2\bar{r}J_0\left(\lambda_0\bar{r}\right)J_1\left(\lambda_0\bar{r}\right)\left[1-\cos\left(\pi\bar{z}/l\right)\right]}{\sqrt{4+92.968(1+5.9504l^2)\kappa^2\bar{r}^2J_1^2\left(\lambda_0\bar{r}\right)\sin^2\left(\frac{1}{2}\pi\bar{z}/l\right)}}\boldsymbol{e}_z\end{aligned} \quad (65)$$

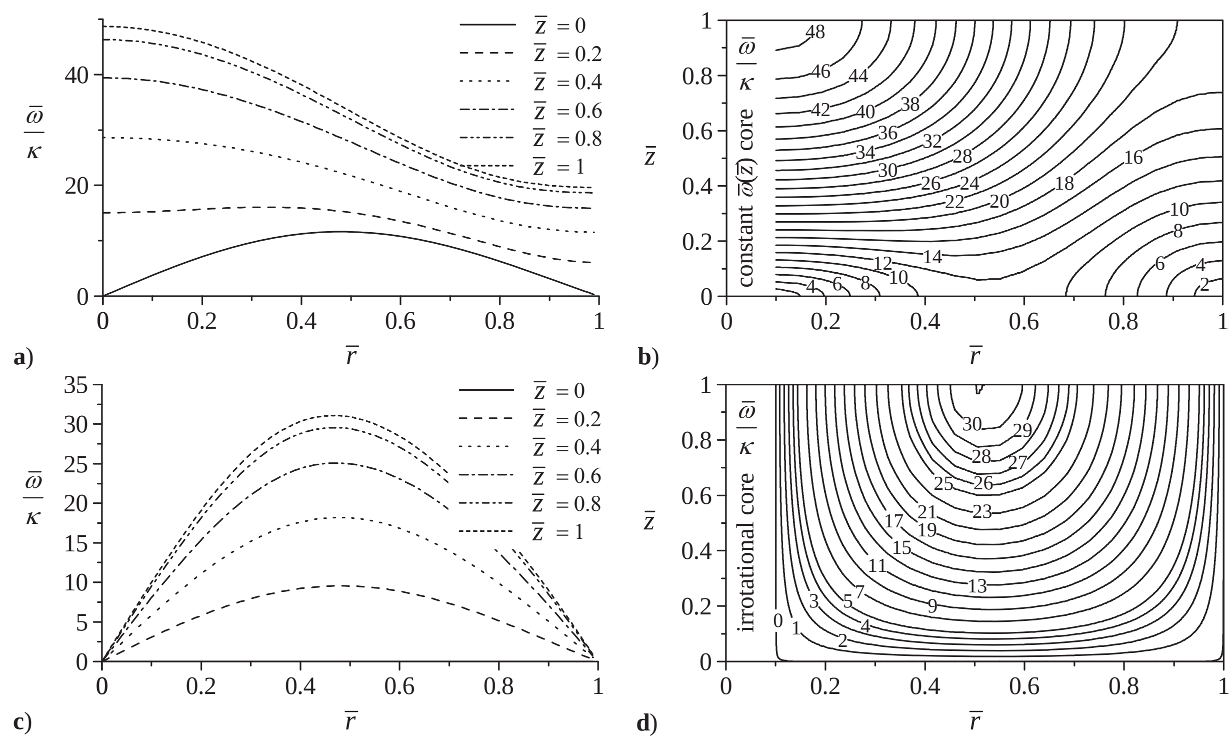

Figure 11. Radial distribution of total vorticity along fixed a) axial positions and b) isolines. The same is repeated in c- d) for the slip permitting solution.

The vorticity and velocity components stemming from Eqs. (61) and (65) may be readily manipulated to verify the vanishing of the Lamb vector which, in effect, is caused by the Beltramian parallelism ascribed to

$$\frac{\bar{\boldsymbol{\omega}}}{\bar{\boldsymbol{u}}} = \lambda_0 \left[1 + \frac{\pi^2}{4\lambda_0^2 l^2} + \frac{1}{c^2\kappa^2\lambda_0^2 l^2 \bar{r}^2 \sin^2\left(\frac{1}{2}\pi\bar{z}/l\right) J_1^2\left(\lambda_0 \bar{r}\right)} \right]^{-1/2} \tag{66}$$

So while $\bar{\boldsymbol{\omega}}$ and $\bar{\boldsymbol{u}}$ retain a fixed relative alignment throughout the chamber, the ratio of relative magnitudes $|\bar{\boldsymbol{\omega}}/\bar{\boldsymbol{u}}|$ varies locally from one point to the other. This feature is, of course, characteristic of a Beltrami flowfield. Note that all of the new models exhibit the property $\bar{\boldsymbol{\omega}}/\bar{\boldsymbol{u}} = \bar{\mathrm{B}}/\bar{\psi}$. Accordingly, the vorticity-to-velocity ratio is identical to the ratio of the tangential angular momentum and the stream function.

In the interest of clarity, a summary of the main equations associated with the case at hand is offered in Table 4. The character of the vorticity is illustrated in Fig. 11 for the two models at hand, using both radial vorticity lines at fixed $\bar{z}$ (in a,c) and isovorticity contours in the $\bar{r}-\bar{z}$ plane (in b,d). These plots may also be compared to those given in Fig. 7 for the $\upsilon = 0$ cases.

Consistently with the velocity and pressure attributes, we find these profiles to produce higher levels of vorticity and distributions that are commensurate with their core vortex evolution. In Figs. 11a,b, it is clear that $\bar{\omega}$ approaches a constant value as $\bar{r} \to 0$. The constant angular rotation of the fluid near the centerline is gratifying, being characteristic of forced vortex motion. It can be seen not only Figs. 11a,b but also, Figs. 7a,b, where the corresponding swirl velocity vanishes at the radial endpoints. In contrast, the trends in Figs. 11c,d appear to be analogous, despite having slightly higher magnitudes than those depicted in Figs. 7c,d. These slip permitting profiles give rise to an irrotational region near the chamber axis where viscous stresses become prevalent. A similar irrotational region appears near the wall where the velocity adherence condition is relaxed.

Despite these deficiencies, the vorticity contours induced here may, at some point, be reconciled with those obtained numerically, with two examples shown in Fig. 12. The main departure from the CFD results appears near the wall where a region of concentrated vorticity is expected to form. Based on these preliminary RSM simulations, it seems possible for the inviscid profiles to provide suitable approximations to the swirl induced bidirectional motions, especially after properly accounting for wall boundary layers.

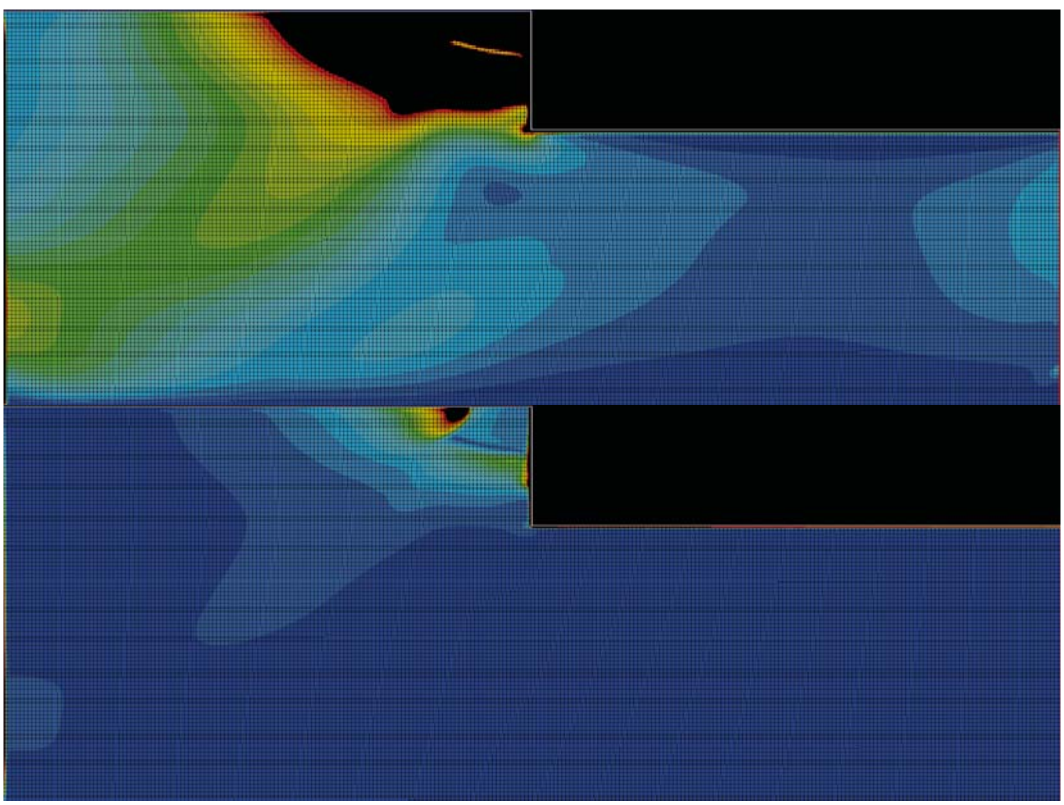

Figure 12. Contours of isovorticity using RSM simulations in a bidirectional vortex tank.

Table 4. Cases of $\upsilon = \frac{1}{2}\pi / L$

Variable	Equation
	Common parts
$\bar{\psi}$	$c\kappa l\,\bar{r}\sin\left(\frac{1}{2}\pi\bar{z}/l\right)J_1\left(\lambda_0\bar{r}\right)$
$(\bar{u}_r)_{\text{cross}}$	$-2.5028\kappa\cos\left(\frac{1}{2}\pi\bar{z}/l\right)$
$(\bar{u}_r)_{\max}$	$-2.8052\kappa\cos\left(\frac{1}{2}\pi\bar{z}/l\right)$
$\dfrac{\partial\bar{p}}{\partial\bar{z}}$	$-\frac{1}{4}\pi c^2\lambda_0^2\kappa^2 l[J_0^2(\lambda_0\bar{r})+J_1^2(\lambda_0\bar{r})]\sin\left(\pi\bar{z}/l\right)$
	Case with no slip
$\bar{\boldsymbol{u}}$	$\begin{cases}-\frac{1}{2}\pi c\kappa\cos\left(\frac{1}{2}\pi\bar{z}/l\right)J_1\left(\lambda_0\bar{r}\right)\boldsymbol{e}_r+c\lambda_0\kappa l\sin\left(\frac{1}{2}\pi\bar{z}/l\right)J_0\left(\lambda_0\bar{r}\right)\boldsymbol{e}_z\\+\frac{1}{2}\pi c\kappa\sqrt{1+4\lambda_0^2l^2/\pi^2}\sin\left(\frac{1}{2}\pi\bar{z}/l\right)J_1\left(\lambda_0\bar{r}\right)\boldsymbol{e}_\theta\end{cases}$
$\bar{\boldsymbol{\omega}}$	$\begin{cases}-\frac{1}{2}c\pi\kappa\sqrt{\lambda_0^2+\frac{1}{4}\pi^2/l^2}J_1\left(\lambda_0\bar{r}\right)\cos\left(\frac{1}{2}\pi\bar{z}/l\right)\boldsymbol{e}_r+c\kappa l(\lambda_0^2+\frac{1}{4}\pi^2/l^2)J_1\left(\lambda_0\bar{r}\right)\sin\left(\frac{1}{2}\pi\bar{z}/l\right)\boldsymbol{e}_\theta\\+c\kappa l\lambda_0\sqrt{\lambda_0^2+\frac{1}{4}\pi^2/l^2}J_0\left(\lambda_0\bar{r}\right)\sin\left(\frac{1}{2}\pi\bar{z}/l\right)\boldsymbol{e}_z\end{cases}$
$(\bar{u}_\theta)_{\max}$	$0.4465\sigma^{-1}\sqrt{l^{-2}+5.9504}\sin\left(\frac{1}{2}\pi\bar{z}/l\right)$
$\dfrac{\partial\bar{p}}{\partial\bar{r}}$	$\frac{1}{4}c^2\kappa^2J_1(\lambda_0\bar{r})\left\{-\pi^2\lambda_0J_0(\lambda_0\bar{r})+\bar{r}^{-1}J_1(\lambda_0\bar{r})\left[\pi^2+2l^2\lambda_0^2-2l^2\lambda_0^2\cos\left(\pi\bar{z}/l\right)\right]\right\}$
$\Delta\bar{p}$	$-\frac{1}{8}c^2\kappa^2\left\{\pi^2\left[1+J_1^2(\lambda_0\bar{r})\right]+2\lambda_0^2l^2[J_0^2(\lambda_0\bar{r})+J_1^2(\lambda_0\bar{r})]\left[1-\cos\left(\pi\bar{z}/l\right)\right]\right\}$
$\tilde{\Omega}$	$\frac{1}{48}\beta\lambda_0^2\sqrt{4\lambda_0^2+\pi^2/l^2}\;{}_2F_3\left[\left(\frac{3}{2},\frac{3}{2}\right),\left(2,2,\frac{5}{2}\right),-\beta^2\lambda_0^2\right]J_1^{-2}\left(\beta\lambda_0\right)\cong 0.549604\sqrt{1+5.9504l^2}$
	Case with slip
$\bar{\boldsymbol{u}}$	$\begin{cases}-\frac{1}{2}\pi c\kappa\cos\left(\frac{1}{2}\pi\bar{z}/l\right)J_1\left(\lambda_0\bar{r}\right)\boldsymbol{e}_r+c\lambda_0\kappa l\sin\left(\frac{1}{2}\pi\bar{z}/l\right)J_0\left(\lambda_0\bar{r}\right)\boldsymbol{e}_z\\+\dfrac{1}{\bar{r}}\sqrt{1+c^2\kappa^2\left(\lambda_0^2l^2+\frac{1}{4}\pi^2\right)\bar{r}^2J_1^2\left(\lambda_0\bar{r}\right)\sin^2\left(\frac{1}{2}\pi\bar{z}/l\right)}\boldsymbol{e}_\theta\end{cases}$
$\bar{\boldsymbol{\omega}}$	$\begin{cases}-\dfrac{c^2\pi\kappa^2(\pi^2+4l^2\lambda_0^2)\bar{r}J_1^2\left(\lambda_0\bar{r}\right)\sin\left(\pi\bar{z}/l\right)}{8l\sqrt{4+c^2\kappa^2(\pi^2+4l^2\lambda_0^2)\bar{r}^2J_1^2\left(\lambda_0\bar{r}\right)\sin^2\left(\frac{1}{2}\pi\bar{z}/l\right)}}\boldsymbol{e}_r+\dfrac{c\kappa}{4l}(\pi^2+4l^2\lambda_0^2)J_1\left(\lambda_0\bar{r}\right)\sin\left(\frac{1}{2}\pi\bar{z}/l\right)\boldsymbol{e}_\theta\\+\dfrac{c^2\lambda_0\kappa^2(\pi^2+4l^2\lambda_0^2)\bar{r}J_0\left(\lambda_0\bar{r}\right)J_1\left(\lambda_0\bar{r}\right)\left[1-\cos\left(\pi\bar{z}/l\right)\right]}{4\sqrt{4+c^2\kappa^2(\pi^2+4l^2\lambda_0^2)\bar{r}^2J_1^2\left(\lambda_0\bar{r}\right)\sin^2\left(\frac{1}{2}\pi\bar{z}/l\right)}}\boldsymbol{e}_z\end{cases}$
$(\bar{u}_\theta)_{\max}$	∞
$\dfrac{\partial\bar{p}}{\partial\bar{r}}$	$\bar{r}^{-3}+\frac{1}{4}c^2\kappa^2J_1(\lambda_0\bar{r})\left\{-\pi^2\lambda_0J_0(\lambda_0\bar{r})+\bar{r}^{-1}J_1(\lambda_0\bar{r})\left[\pi^2+2l^2\lambda_0^2-2l^2\lambda_0^2\cos\left(\pi\bar{z}/l\right)\right]\right\}$
$\Delta\bar{p}$	$-\frac{1}{2}\bar{r}^{-2}-\frac{1}{8}c^2\kappa^2\left\{\pi^2\left[1+J_1^2(\lambda_0\bar{r})\right]+2\lambda_0^2l^2[J_0^2(\lambda_0\bar{r})+J_1^2(\lambda_0\bar{r})]\left[1-\cos\left(\pi\bar{z}/l\right)\right]\right\}$

V. Solutions with Sidewall Injection

A. Extended Boundary Conditions

The solutions presented heretofore can be modified to the extent of accounting for sidewall mass injection. Such a problem arises in the modeling of hybrid rocket internal gas dynamics. The Vortex Injection Hybrid Rocket Engine represents one such case in which wall blowing is induced by the inward ejection of gases into a bidirectional vortex flowfield. The original problem was conceived and resolved by Majdalani and Vyas,[32] and later restructured to incorporate multidirectional boundary layer corrections by Majdalani.[33] The main departure from the hardwall problem lies in prescribing a surface boundary condition that captures the effects of sidewall injection. This is achieved by replacing Eq. (9)c by $u_r(a,z) = -U_w$, where U_w denotes the effective blowing speed at the wall. Moreover, the expression for mass conservation may be expanded to account for the secondary wall influx. This can be accomplished by setting

$$\int_0^{2\pi}\int_0^b \boldsymbol{u}(r,L)\cdot\boldsymbol{n}\, r\mathrm{d}r\mathrm{d}\theta = 2\pi\int_0^b u_z(r,L)\, r\mathrm{d}r = Q_{in} = Q_i + Q_w = UA_i + 2\pi a L U_w \tag{67}$$

The first two boundary conditions in Eqs. (9)a-b act to suppress axial flow at the headwall and radial speed at the centerline. These conditions can be utilized to transform Eq. (8) into

$$\psi(r,z) = \begin{cases} \psi_0 z r J_1(rC_n); \quad \upsilon = 0 & (a) \\ \psi_0 r \sin(\upsilon z) J_1(r\sqrt{C_n^2 - \upsilon^2}); \quad C_n^2 > \upsilon^2 & (b) \end{cases} \tag{68}$$

where the hypergeometric form is deliberately ignored while the remaining solutions are denoted by (a) and (b), sequentially. At this point, global conservation through Eq. (67) may be carried out to retrieve

$$\psi_0 = \begin{cases} \dfrac{Q_{in}}{2\pi a\beta L J_1\left(bC_n\right)} & (a) \\[2ex] \dfrac{Q_{in}}{2\pi a\beta J_1\left(b\sqrt{C_n^2 - \frac{1}{4}\pi^2/L^2}\right)} & (b) \end{cases} \tag{69}$$

To satisfy the spatially uniform constraint $u_r(a,z) = -U_w$, it is required that

$$\begin{cases} \psi_0 J_1(C_n a) = U_w & (a) \\ \psi_0 \upsilon \cos(\upsilon z) J_1(a\sqrt{C_n^2 - \upsilon^2}) = U_w & (b) \end{cases} \tag{70}$$

Note that the second member of Eq. (70) cannot be secured unless the blowing velocity is cosine-harmonic, namely of the form $u_r(a,z) = -U_w\cos(\upsilon z)$. Then given the endwall restraint $u_r(r,L) = 0$, one deduces the necessity of selecting $\upsilon = \frac{1}{2}\pi/L$. A solution for a wall injection distribution of $u_r(a,z) = -U_w\cos(\frac{1}{2}\pi z/L)$ can therefore be accommodated by the axially harmonic profile. The contiguous pair of wall boundary conditions that seem appropriate of this problem become

$$u_r(a,z) = \begin{cases} -U_w; \quad \upsilon = 0 & (a) \\ -U_w\cos(\frac{1}{2}\pi z/L); \quad \upsilon = \frac{1}{2}\pi/L & (b) \end{cases} \tag{71}$$

Evidently, other forms of wall injection patterns may be prescribed but these are not considered here.

B. Stream Function Formulation

Imposing Eq. (71) leads to

$$\begin{cases} \dfrac{Q_{in}}{2\pi bL}\dfrac{J_1(aC_n)}{J_1\left(bC_n\right)} = U_w & (a) \\[2ex] \dfrac{Q_{in}}{4bL}\dfrac{J_1(a\sqrt{C_n^2 - \frac{1}{4}\pi^2/L^2})}{J_1\left(b\sqrt{C_n^2 - \frac{1}{4}\pi^2/L^2}\right)} = U_w & (b) \end{cases} \tag{72}$$

These could be expanded using

$$\begin{cases} \dfrac{Q_i + 2\pi a L U_w}{2\pi bL}\dfrac{J_1(aC_n)}{J_1\left(bC_n\right)} = U_w \\[2ex] \dfrac{Q_i + 2\pi a L U_w}{4bL}\dfrac{J_1(a\sqrt{C_n^2 - \frac{1}{4}\pi^2/L^2})}{J_1\left(b\sqrt{C_n^2 - \frac{1}{4}\pi^2/L^2}\right)} = U_w \end{cases} \quad \text{or} \quad \begin{cases} \left(\kappa U + U_w\right)\dfrac{J_1(aC_n)}{\beta J_1\left(bC_n\right)} = U_w \\[2ex] \dfrac{\pi}{2}\left(\kappa U + U_w\right)\dfrac{J_1(a\sqrt{C_n^2 - \frac{1}{4}\pi^2/L^2})}{\beta J_1\left(b\sqrt{C_n^2 - \frac{1}{4}\pi^2/L^2}\right)} = U_w \end{cases} \tag{73}$$

where group parameters leading to κ and β have been collected. The emergence of the characteristic velocities in the right-hand-side expressions prompts us to divide through by U and rearrange. Then using $\varepsilon = U_w/U$, we are left with

$$\begin{cases}\dfrac{J_1(aC_n)}{J_1(bC_n)} = \dfrac{\varepsilon\beta}{\kappa+\varepsilon} & (a)\\[2ex] \dfrac{J_1\left(a\sqrt{C_n^2-\frac{1}{4}\pi^2/L^2}\right)}{J_1\left(b\sqrt{C_n^2-\frac{1}{4}\pi^2/L^2}\right)} = \dfrac{2}{\pi}\dfrac{\varepsilon\beta}{\kappa+\varepsilon} & (b)\end{cases} \quad \text{or} \quad \frac{J_1(\lambda_n)}{J_1(\beta\lambda_n)} = \begin{cases} \dfrac{\varepsilon\beta}{\kappa+\varepsilon}; \quad C_n = \dfrac{\lambda_n}{a} & (a)\\[2ex] \dfrac{2}{\pi}\dfrac{\varepsilon\beta}{\kappa+\varepsilon}; \quad C_n=\sqrt{\dfrac{\lambda_n^2}{a^2}+\dfrac{\pi^2}{4L^2}} & (b)\end{cases} \tag{74}$$

This expression enables us to obtain multiple solutions for λ_n at fixed open fraction β, sidewall injection ratio ε, and tangential inflow parameter κ. Using λ_0 to define the lowest root of Eq. (74) that is associated with the development of a single mantle, it is possible to numerically obtain the universe of solutions $\lambda_0 = \lambda_0(\beta,\varepsilon,\kappa)$ directly from

$$\frac{J_1(\lambda_0)}{J_1(\beta\lambda_0)} = \left\{ \frac{\varepsilon\beta}{\kappa+\varepsilon}; \quad C_0 = \frac{\lambda_0}{a} \qquad (a); \qquad \frac{2}{\pi}\frac{\varepsilon\beta}{\kappa+\varepsilon}; \quad C_0 = \sqrt{\frac{\lambda_0^2}{a^2}+\frac{\pi^2}{4L^2}} \qquad (b) \right\} \tag{75}$$

where β depends on the relative size of the geometric outlet. The resulting stream function becomes

$$\psi(r,z) = \begin{cases} \dfrac{Q_{in}}{2\pi a\beta L J_1(\beta\lambda_0)} zrJ_1\left(\dfrac{\lambda_0 r}{a}\right) = \dfrac{\kappa U + U_w}{\beta J_1(\beta\lambda_0)} rzJ_1\left(\dfrac{\lambda_0 r}{a}\right) & (a)\\[2ex] \dfrac{Q_{in}}{2\pi a\beta J_1(\beta\lambda_0)} r\sin\left(\dfrac{\pi z}{2L}\right) J_1\left(\dfrac{\lambda_0 r}{a}\right) = L\dfrac{\kappa U + U_w}{\beta J_1(\beta\lambda_0)} r\sin\left(\dfrac{\pi z}{2L}\right) J_1\left(\dfrac{\lambda_0 r}{a}\right) & (b)\end{cases} \tag{76}$$

and so, in dimensionless form,

$$\bar\psi(\bar r,\bar z) = \begin{cases} \dfrac{\kappa+\varepsilon}{\beta J_1(\beta\lambda_0)} \bar r\bar z J_1(\lambda_0\bar r) & (a)\\[2ex] \dfrac{\kappa+\varepsilon}{\beta J_1(\beta\lambda_0)} l\bar r \sin\left(\dfrac{\pi\bar z}{2l}\right) J_1(\lambda_0\bar r) & (b)\end{cases} \quad \text{or} \quad \bar\psi(\bar r,\bar z) = \begin{cases} c\kappa_\varepsilon \bar r\bar z J_1(\lambda_0\bar r) & (a)\\ c\kappa_\varepsilon l\bar r \sin\left(\frac{1}{2}\pi\bar z/l\right) J_1(\lambda_0\bar r) & (b)\end{cases} \tag{77}$$

where $$\kappa_\varepsilon \equiv \kappa+\varepsilon \quad \text{and} \quad c \equiv 1/[\beta J_1(\beta\lambda_0)] \tag{78}$$

In view of the perfect similarity that stands between Eq. (77) and the stream functions with no sidewall injection, the

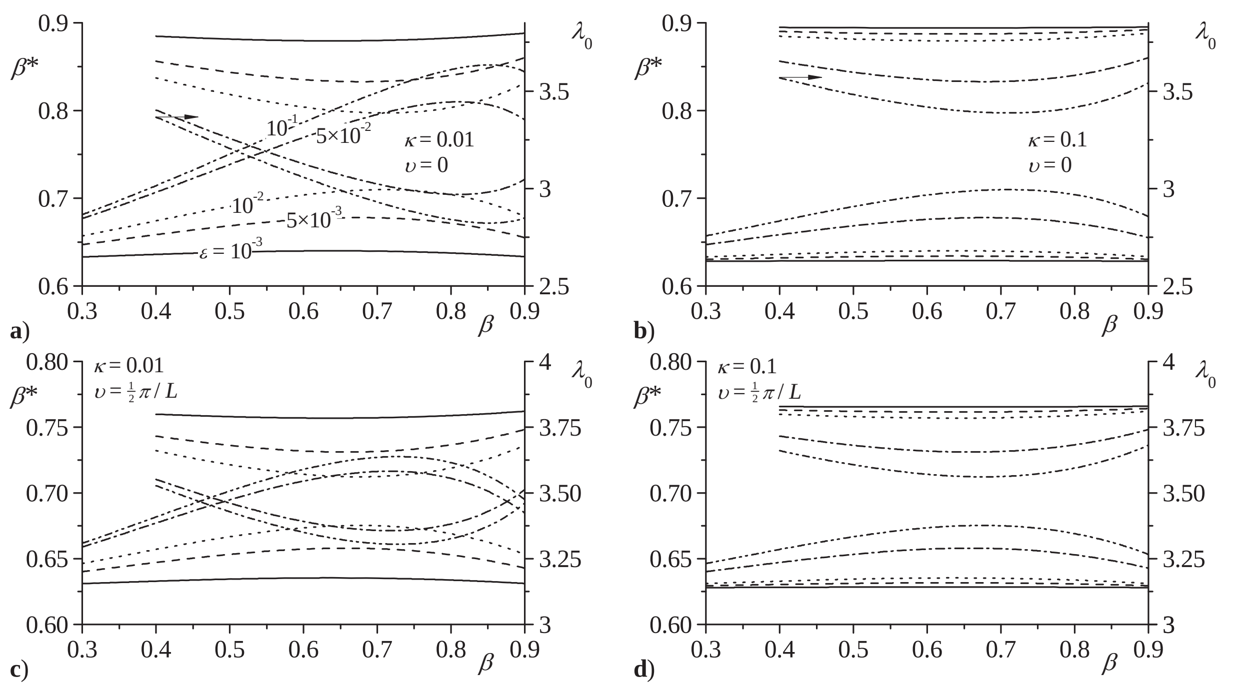

Figure 13. Variation of the mantle location β^* and corresponding eigenvalue λ_0 as function of the chamber's open fraction β. Results are shown for several values of the sidewall injection ratio ε and two fixed values of the tangential inflow parameter κ.

key formulations for the various cases that may be explored need not be re-derived. Their final outcome may be arrived at directly by replacing the impermeable κ by κ_ε. The other difference consists of allowing λ_0 and β^* to vary as per Eq. (75).

C. Mantle Sensitivity to Sidewall Injection, Open Outlet Fraction, and Inflow Parameter

The mantle with sidewall blowing may be located, just as usual,[33] by setting $\bar{u}_z(\beta^*, \bar{z}) = 0$. This translates into

$$J_0\left(\lambda_0\beta^*\right) = 0 \quad \text{or} \quad \beta^* = \frac{j_0}{\lambda_0} = \frac{2.40482556}{\lambda_0} \tag{79}$$

where j_0 is the appropriate root of $J_0\left(j_0\right) = 0$. In general, given a chamber design specific β, λ_0 can be computed from Eq. (75) (at fixed ε and κ), and then inserted into Eq. (79) to retrieve the mantle location. For example, when conditions correspond to $\beta = 0.7$, $\varepsilon = 0.01$ and $\kappa = 0.125$, one calculates, for $\upsilon = 0$, $\lambda_0 = 3.77302$, and $\beta^* = 0.637375$; the same analysis for $\upsilon = \frac{1}{2}\pi / L$ yields a slightly higher value of $\lambda_0 = 3.79461$, and a lower value of $\beta^* = 0.633748$.

The mantle's dependence on β, ε, λ_0, κ, and υ, is illustrated in Fig. 13 where the variation of both β^* (left scale) and λ_0 (right scale) versus β are displayed on one graph. Results are shown along 5 constant sidewall injection lines corresponding to $\varepsilon = 10^{-3}, 5\times10^{-3}, 10^{-2}, 5\times10^{-2}$, and 10^{-1} using a) $\kappa = 0.01, \upsilon = 0$, b) $\kappa = 0.1, \upsilon = 0$, c) $\kappa = 0.01, \upsilon = \frac{1}{2}\pi / L$, and d) $\kappa = 0.1, \upsilon = \frac{1}{2}\pi / L$. At the outset, it may be inferred that increasing κ relative to ε reduces the variability of the mantle location. This can be attributed to the asymptotic nature of the right-hand-side of Eq. (75). Conversely, increasing ε leads to a heightened sensitivity of β^* to small variations in

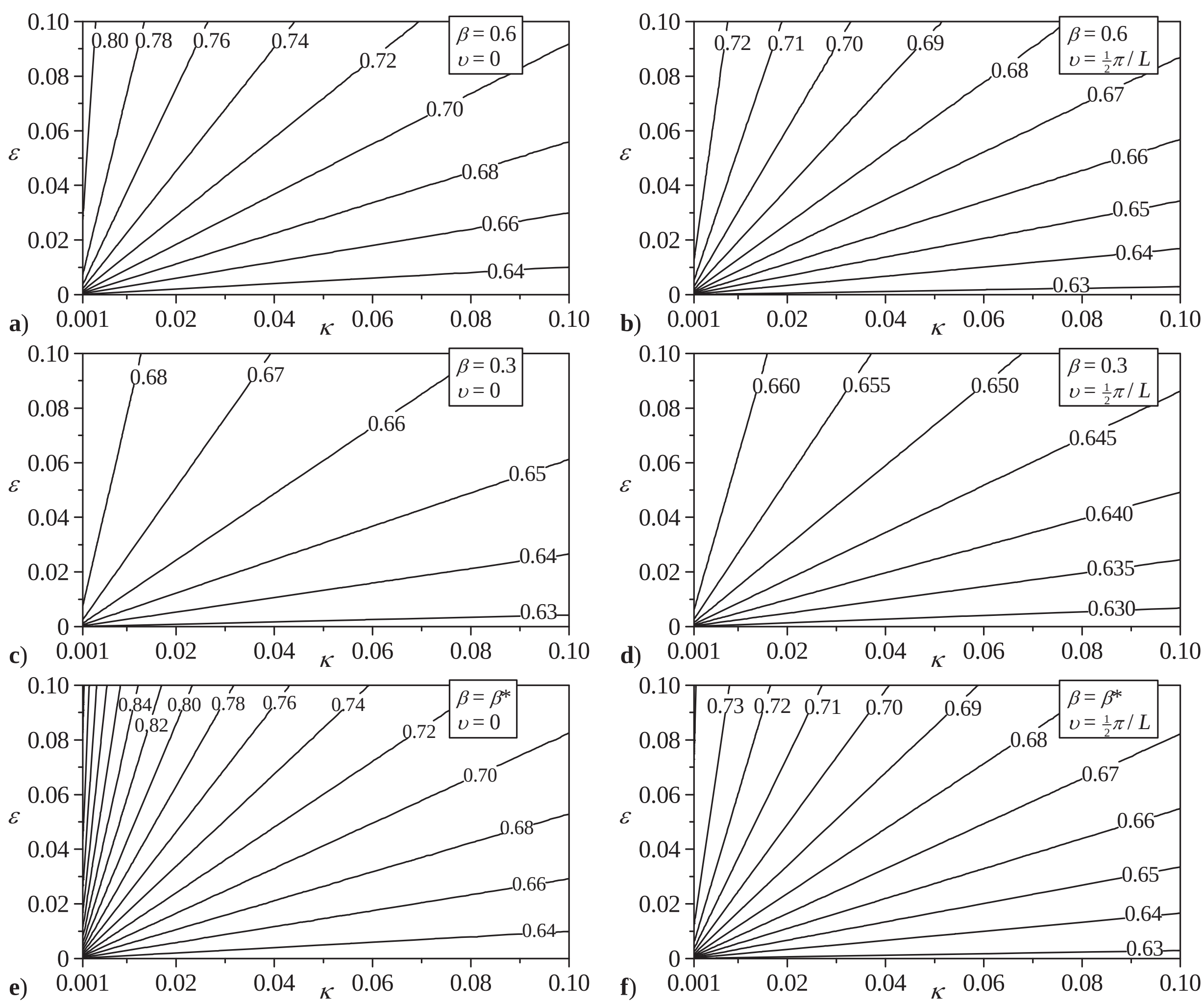

Figure 14. Iso-parametric variation of the mantle position β^* with ε and κ given a-b) β=0.6, c-d) β=0.3, and β=β^*.

β. Common to all four cases shown, β^* first increases with β, reaches a peak value at $\beta = \beta^*$, and then declines with further increases in the open outlet fraction. For $\varepsilon \le 10^{-4}$ (not shown) a flattening of the β and λ_0 curves occurs as the solution levels off to the constant mantle location associated with the hardwall configuration. We hence recover flat lines at $\beta^* = 0.627612$ and $\lambda_0 = 3.8317$.

To further elucidate the mantle's variability with the tangential inflow and sidewall injection parameters, contour plots of constant β^* are provided in Fig. 14 for the two cases at hand. This parametric study is carried out over a wide range of ε and κ, albeit at fixed values of the open outlet fraction, $\beta = 0.6$ (a,b), $\beta = 0.3$ (c,d), and $\beta = \beta^*$ (e,f). Nonetheless, the results for the (a-d) cases are characteristic of a typical geometric opening β. They clearly show that: (i) increasing either ε at constant κ leads to an outward shift in the mantle; (ii) decreasing κ (i.e. increasing swirl) at constant ε leads to an outward shift in the mantle; (iii) at any fixed ε or κ, $\beta^*_{\upsilon=0} > \beta^*_{\upsilon=\frac{1}{2}\pi/L}$; (iv) constricting the geometric opening β plays an appreciable role in reducing the sensitivity of the mantle to inlet and sidewall injection levels.

Graphically, it may be easily surmised that the excursion range of β^* is considerably diminished when β is decreased. The converse is true in that the variability of β^* is expanded, at least in theory, when the outlet opening is progressively enlarged. On this note, it may be instructive to recall that several other investigators have reported similar shifting in mantle positioning due to geometric modifications influencing their outlets. In the context of cyclone separators, the experimental bias caused by changing the diameter of the vortex finder is well known and has been widely reported in the literature.[16-19] These include the work of Smith[11-12] cited earlier in this study.

For the purpose of simplification, one may set $\beta = \beta^*$, thus envisioning a geometric outlet radius that tracks and matches the mantle's radius.[33] This idea was introduced by Majdalani and Vyas[32] with the intent of eliminating irregularities that may arise at $z = L$, such as collisions and recirculatory cells. The same idealization also leads to a fluid dynamically consistent model in which the axial annular flow that spirals toward the headwall from positive infinity (i.e., the axial source at $z = L$,) is permitted to naturally reverse direction and return unencumbered, through the inner vortex region, to positive infinity. By setting $\beta = \beta^*$, we are effectively ensuring that the diameter of the inner vortex matches the diameter of the open boundary at $z = L$. We are also capturing the peak values reported on Fig. 13. For this hypothetical setting, Eq. (75) simplified into:

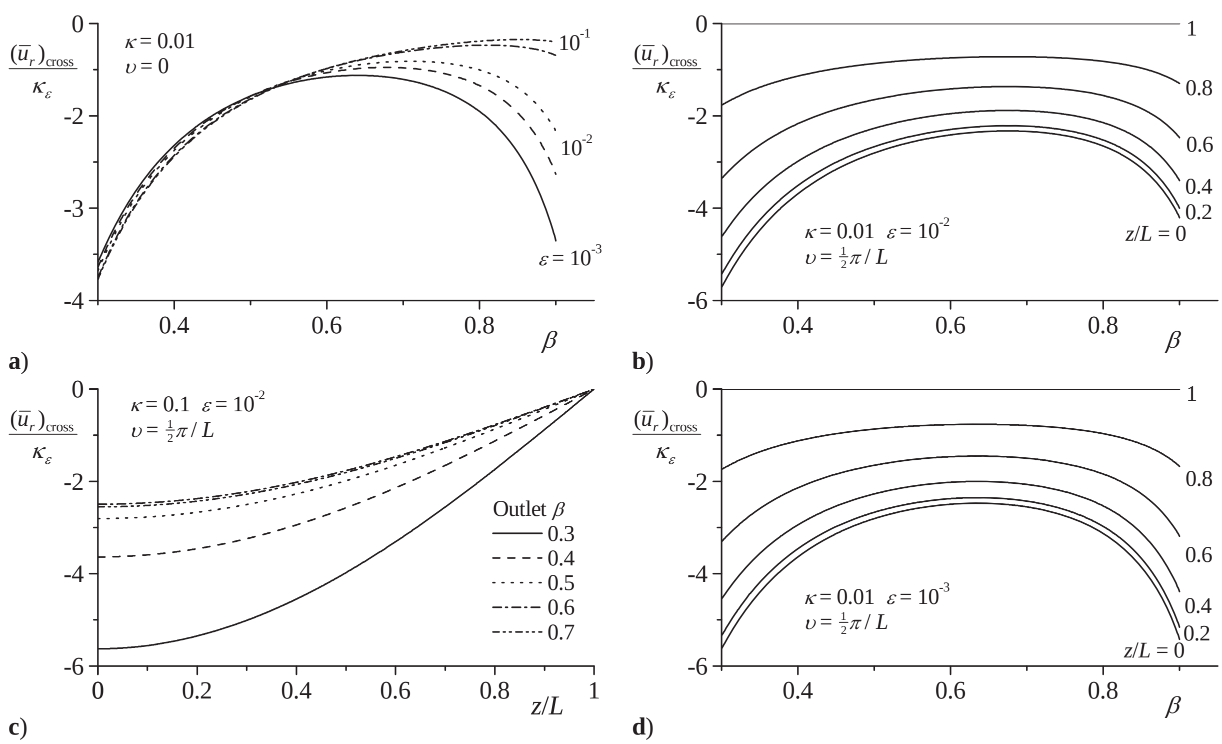

Figure 15. Variation of the crossflow velocity with β and ε. While the case of $\upsilon = 0$ is featured in a), parts c-d) correspond to the $\upsilon = \frac{1}{2}\pi / L$ solution. The latter requires additional analysis due to its spatial dependence.

$$\beta = \beta^* = \frac{j_0}{\lambda_0}; \qquad \frac{\lambda_0 J_1(\lambda_0)}{j_0 J_1(j_0)} = \begin{cases} \dfrac{\varepsilon}{\kappa+\varepsilon} & (a) \\ \dfrac{2}{\pi}\dfrac{\varepsilon}{\kappa+\varepsilon} & (b) \end{cases} \tag{80}$$

Figures 14e,f display the contours of β^* over a full range of ε and κ. In comparison to the previously featured cases of Figs. 14a-d, the mantle offset is not only the largest of the group but also the most widespread. Here too, we confirm that $\beta^*_{\upsilon=0} > \beta^*_{\upsilon=\frac{1}{2}\pi/L}$.

In addition to the $\beta = \beta^*$ configuration, a practical scenario that is worth investigating consists of fixing the outlet radius to a design-specific value. In the absence of user input, the logical choice would be to set $\beta = 0.6276$, being the lowest β^* that the mantle can tolerate in the limit of $\varepsilon \to 0$. In either configurations, solutions may be obtained straightforwardly from Eq. (77).

D. Other characteristic Properties

Despite the mantle's elusive parametric sensitivity, the crossflow velocity can be readily obtained from

$$(\bar{u}_r)_{\text{cross}} = \begin{cases} -\kappa_\varepsilon \dfrac{J_1(\lambda_0\beta^*)}{\beta J_1(\beta\lambda_0)} & (a) \\ -\frac{1}{2}\pi\kappa_\varepsilon \cos\left(\frac{1}{2}\pi\bar{z}/l\right)\dfrac{J_1(\lambda_0\beta^*)}{\beta J_1(\beta\lambda_0)} & (b) \end{cases} \tag{81}$$

Due to the axial invariance of Eq. (81)a, its behavior is fully captured in Fig. 15a, albeit at a single value of κ. Interestingly, the crossflow is considerably increased when the outlet fraction is reduced. In fact, it becomes very weakly dependent on ε for approximately $\beta < 0.55$. The axially harmonic solution is featured in Figs. 15b-d

Table 5. Sidewall injection cases with $\upsilon = 0$

Variable	Equation
	Common parts
$\bar{\psi}$	$c\kappa_\varepsilon \bar{z}\,\bar{r} J_1(\lambda_0\bar{r})$
$\bar{u}_r$	$-c\kappa_\varepsilon J_1(\lambda_0\bar{r})$
$\bar{u}_z$	$c\lambda_0\kappa_\varepsilon \bar{z} J_0(\lambda_0\bar{r})$
$\dfrac{\partial\bar{p}}{\partial\bar{z}}$	$-c^2\lambda_0^2\kappa_\varepsilon^2\bar{z}[J_0^2(\lambda_0\bar{r}) + J_1^2(\lambda_0\bar{r})]$
	Case with no slip
$\bar{u}_\theta$	$c\lambda_0\kappa_\varepsilon\bar{z}J_1(\lambda_0\bar{r})$
$\bar{\boldsymbol{\omega}}$	$-c\lambda_0\kappa_\varepsilon J_1(\lambda_0\bar{r})\boldsymbol{e}_r + c\lambda_0^2\kappa_\varepsilon\bar{z}J_1(\lambda_0\bar{r})\boldsymbol{e}_\theta + c\lambda_0^2\kappa_\varepsilon\bar{z}J_0(\lambda_0\bar{r})\boldsymbol{e}_z$
$\dfrac{\partial\bar{p}}{\partial\bar{r}}$	$c^2\kappa_\varepsilon^2\left[(1+\lambda_0^2\bar{z}^2)\bar{r}^{-1}J_1^2(\lambda_0\bar{r}) - \lambda_0 J_1(\lambda_0\bar{r})J_0(\lambda_0\bar{r})\right]$
$\Delta\bar{p}$	$-\frac{1}{2}c^2\kappa_\varepsilon^2\{J_1^2(\lambda_0\bar{r}) + \lambda_0^2\bar{z}^2[J_0^2(\lambda_0\bar{r}) + J_1^2(\lambda_0\bar{r})]\}$
	Case with slip
$\bar{u}_\theta$	$\dfrac{1}{\bar{r}}\sqrt{1+c^2\lambda_0^2\kappa_\varepsilon^2\bar{r}^2\bar{z}^2J_1^2(\lambda_0\bar{r})}$
$\bar{\boldsymbol{\omega}}$	$-\dfrac{c^2\lambda_0^2\kappa_\varepsilon^2\bar{r}\bar{z}J_1^2(\lambda_0\bar{r})}{\sqrt{1+c^2\lambda_0^2\kappa_\varepsilon^2\bar{r}^2\bar{z}^2J_1^2(\lambda_0\bar{r})}}\boldsymbol{e}_r + c\lambda_0^2\kappa_\varepsilon\bar{z}J_1(\lambda_0\bar{r})\boldsymbol{e}_\theta + \dfrac{c^2\lambda_0^3\kappa_\varepsilon^2\bar{r}\bar{z}^2J_0(\lambda_0\bar{r})J_1(\lambda_0\bar{r})}{\sqrt{1+c^2\lambda_0^2\kappa_\varepsilon^2\bar{r}^2\bar{z}^2J_1^2(\lambda_0\bar{r})}}\boldsymbol{e}_z$
$\dfrac{\partial\bar{p}}{\partial\bar{r}}$	$\bar{r}^{-3} + c^2\kappa_\varepsilon^2\left[(1+\lambda_0^2\bar{z}^2)\bar{r}^{-1}J_1^2(\lambda_0\bar{r}) - \lambda_0J_1(\lambda_0\bar{r})J_0(\lambda_0\bar{r})\right]$
$\Delta\bar{p}$	$-\frac{1}{2}\bar{r}^{-2} - \frac{1}{2}c^2\kappa_\varepsilon^2\{J_1^2(\lambda_0\bar{r}) + \lambda_0^2\bar{z}^2[J_0^2(\lambda_0\bar{r}) + J_1^2(\lambda_0\bar{r})]\}$

where its axial variation is illustrated. Here too, reducing the outlet fraction seems to induce an increase in the absolute magnitude of the crossflow along the mantle. For the ideal case of $\beta=\beta^*$, Eq. (81) reduces to:

$$\frac{(\bar{u}_r)_{\text{cross}}}{\kappa_\varepsilon}=\begin{cases}-\dfrac{1}{\beta} & (a)\\[2ex] -\dfrac{\pi}{2\beta}\cos\left(\tfrac{1}{2}\pi\bar{z}/l\right) & (b)\end{cases} \tag{82}$$

Equation (82) reminds us of the expressions posted in Tables 3 and 4 in which the crossflow velocity for the no-wall injection case are listed. Those entries can be recovered from Eq. (82) by replacing κ_ε by κ and β by 0.627612. The converse is also true of other characteristic flow attributes by virtue of the parental role that the stream function plays in Eq. (77). In avoidance of a lengthy derivation that is duplicative of steps that have been thoroughly outlined in Secs. II-IV, a summary of the key features of the bidirectional vortex with sidewall injection are catalogued and listed in Tables 5 and 6. In forthcoming work, most of these features will be thoroughly explored in the context of a boundary layer treatment that seeks to overcome the intransigent singularities and deficiencies of inviscid motions. Additionally, an asymptotic approach will be presented as an alternate avenue for capturing the secondary effects of sidewall mass injection.

Table 6. Sidewall injection case with $\upsilon=\frac{1}{2}\pi/L$

Variable	Equation
	Common parts
$\bar{\psi}$	$c\kappa_\varepsilon l\bar{r}\sin\left(\tfrac{1}{2}\pi\bar{z}/l\right)J_1\left(\lambda_0\bar{r}\right)$
$\bar{u}_r$	$-\tfrac{1}{2}\pi c\kappa_\varepsilon\cos\left(\tfrac{1}{2}\pi\bar{z}/l\right)J_1\left(\lambda_0\bar{r}\right)$
$\bar{u}_z$	$c\lambda_0\kappa_\varepsilon l\sin\left(\tfrac{1}{2}\pi\bar{z}/l\right)J_0\left(\lambda_0\bar{r}\right)$
$\dfrac{\partial\bar{p}}{\partial\bar{z}}$	$-\tfrac{1}{4}\pi c^2\lambda_0^2\kappa_\varepsilon^2 l[J_0^2(\lambda_0\bar{r})+J_1^2(\lambda_0\bar{r})]\sin\left(\pi\bar{z}/l\right)$
	Case with no slip
$\bar{u}_\theta$	$\tfrac{1}{2}\pi c\kappa_\varepsilon\sqrt{1+4\lambda_0^2l^2/\pi^2}\sin\left(\tfrac{1}{2}\pi\bar{z}/l\right)J_1\left(\lambda_0\bar{r}\right)$
$\bar{\boldsymbol{\omega}}$	$\begin{cases}-\tfrac{1}{2}c\pi\kappa_\varepsilon\sqrt{\lambda_0^2+\tfrac{1}{4}\pi^2/l^2}\,J_1\left(\lambda_0\bar{r}\right)\cos\left(\tfrac{1}{2}\pi\bar{z}/l\right)\boldsymbol{e}_r+c\kappa_\varepsilon l(\lambda_0^2+\tfrac{1}{4}\pi^2/l^2)J_1\left(\lambda_0\bar{r}\right)\sin\left(\tfrac{1}{2}\pi\bar{z}/l\right)\boldsymbol{e}_\theta\\ +c\kappa_\varepsilon l\lambda_0\sqrt{\lambda_0^2+\tfrac{1}{4}\pi^2/l^2}\,J_0\left(\lambda_0\bar{r}\right)\sin\left(\tfrac{1}{2}\pi\bar{z}/l\right)\boldsymbol{e}_z\end{cases}$
$\dfrac{\partial\bar{p}}{\partial\bar{r}}$	$\tfrac{1}{4}c^2\kappa_\varepsilon^2J_1(\lambda_0\bar{r})\left\{-\pi^2\lambda_0J_0(\lambda_0\bar{r})+\bar{r}^{-1}J_1(\lambda_0\bar{r})\left[\pi^2+2l^2\lambda_0^2-2l^2\lambda_0^2\cos\left(\pi\bar{z}/l\right)\right]\right\}$
$\Delta\bar{p}$	$-\tfrac{1}{8}c^2\kappa_\varepsilon^2\left\{\pi^2\left[1+J_1^2(\lambda_0\bar{r})\right]+2\lambda_0^2l^2[J_0^2(\lambda_0\bar{r})+J_1^2(\lambda_0\bar{r})]\left[1-\cos\left(\pi\bar{z}/l\right)\right]\right\}$
	Case with slip
$\bar{u}_\theta$	$\dfrac{1}{\bar{r}}\sqrt{1+c^2\kappa_\varepsilon^2\left(\lambda_0^2l^2+\tfrac{1}{4}\pi^2\right)\bar{r}^2J_1^2\left(\lambda_0\bar{r}\right)\sin^2\left(\tfrac{1}{2}\pi\bar{z}/l\right)}$
$\bar{\boldsymbol{\omega}}$	$\begin{cases}-\dfrac{c^2\pi\kappa_\varepsilon^2(\pi^2+4l^2\lambda_0^2)\bar{r}J_1^2\left(\lambda_0\bar{r}\right)\sin\left(\pi\bar{z}/l\right)}{8l\sqrt{4+c^2\kappa_\varepsilon^2(\pi^2+4l^2\lambda_0^2)\bar{r}^2J_1^2\left(\lambda_0\bar{r}\right)\sin^2\left(\tfrac{1}{2}\pi\bar{z}/l\right)}}\boldsymbol{e}_r+\dfrac{c\kappa_\varepsilon}{4l}(\pi^2+4l^2\lambda_0^2)J_1\left(\lambda_0\bar{r}\right)\sin\left(\tfrac{1}{2}\pi\bar{z}/l\right)\boldsymbol{e}_\theta\\ +\dfrac{c^2\lambda_0\kappa_\varepsilon^2(\pi^2+4l^2\lambda_0^2)\bar{r}J_0\left(\lambda_0\bar{r}\right)J_1\left(\lambda_0\bar{r}\right)\left[1-\cos\left(\pi\bar{z}/l\right)\right]}{4\sqrt{4+c^2\kappa_\varepsilon^2(\pi^2+4l^2\lambda_0^2)\bar{r}^2J_1^2\left(\lambda_0\bar{r}\right)\sin^2\left(\tfrac{1}{2}\pi\bar{z}/l\right)}}\boldsymbol{e}_z\end{cases}$
$\dfrac{\partial\bar{p}}{\partial\bar{r}}$	$\bar{r}^{-3}+\tfrac{1}{4}c^2\kappa_\varepsilon^2J_1(\lambda_0\bar{r})\left\{-\pi^2\lambda_0J_0(\lambda_0\bar{r})+\bar{r}^{-1}J_1(\lambda_0\bar{r})\left[\pi^2+2l^2\lambda_0^2-2l^2\lambda_0^2\cos\left(\pi\bar{z}/l\right)\right]\right\}$
$\Delta\bar{p}$	$-\tfrac{1}{2}\bar{r}^{-2}-\tfrac{1}{8}c^2\kappa_\varepsilon^2\left\{\pi^2\left[1+J_1^2(\lambda_0\bar{r})\right]+2\lambda_0^2l^2[J_0^2(\lambda_0\bar{r})+J_1^2(\lambda_0\bar{r})]\left[1-\cos\left(\pi\bar{z}/l\right)\right]\right\}$

VI. Conclusions

In this study, the Bragg-Hawthorne equation in cylindrical coordinates is used to derive new inviscid models of the bidirectional vortex with and without sidewall injection. The analysis complements a companion study by Barber and Majdalani[41] in which the spherical BHE was solved in the context of cyclonic motion in a conical chamber. By granting the tangential angular momentum the freedom to vary with the stream function, several solutions are derived under steady, inviscid, rotational and incompressible fluid conditions that warrant the invariance of the total pressure along streamlines. In such an isentropic environment, our results are compared to one another and to a previous model obtained via the vorticity-stream function approach. Despite common features that these solutions share, they seem to exhibit slightly different characteristics. These affect their minima and maxima, mantle location, crossflow velocity, pressure distributions, pressure gradients, vorticity, and swirl intensity. The main advantage of the new solutions may be connected with their swirl velocity exhibiting a physically realizable axial dependence, on their non-zero vorticity in all three directions, and on their alternate mantle location which seems to agree with an existing set of reported simulations and experimental measurements. Some of these reports suggest that mantle positioning can also be influenced by the shape, size, and placement of the outlet section or vortex finder. For this reason, an effort to characterize the impact of the chamber's exit opening on the flow behavior has been carried out, for the first time, based on the extended solution with sidewall injection. For each family of solutions developed here, we have attempted to either impose or relax the no-slip requirement at the sidewall. This has led to two classes of self-similar solutions that exhibit dissimilar behavior. The first, no-slip preserving motions, were found to not only vanish at the sidewall, but also along the centerline where a virtual forced vortex region is formed. This somewhat perplexing result led to Trkalian profiles that exhibited swirling speeds that qualitatively agreed with numerical simulations. The second, slip permitting profiles, were substantially dominated by the free vortex motion that emerged from their analysis. These led to Beltramian profiles with identical radial pressure gradients and pressure variations when compared to each other and to the former, complex lamellar profile obtained by Vyas and Majdalani.[29] These will require a separate asymptotic treatment along with a systematic boundary layer analysis that is hoped to be pursued in order to suppress their core and wall singularities. Moreover, any further exploration of this problem will substantially benefit from the production of additional experimental and numerical data. These should be derived from physical models that correspond, as closely as possible, to the idealized configuration considered here.

Acknowledgments

This project was funded by the National Science Foundation through grant No. CMMI-0353518, Dr Eduardo A. Misawa, Program Director.

References

[1]Gloyer, P. W., Knuth, W. H., and Goodman, J., "Overview of Initial Research into the Effects of Strong Vortex Flow on Hybrid Rocket Combustion and Performance," CSTAR Fifth Annual Symposium Paper N96- 16953, January 1993.

[2]Knuth, W. H., Bemowski, P. A., Gramer, D. J., Majdalani, J., and Rothbauer, W. J., "Gas-Fed, Vortex Injection Hybrid Rocket Engine," NASA Marshall Space Flight Center, SBIR Phase I Final Technical Rept. NASA/MSFC Contract NAS8-40679, Huntsville, AL, August 1996.

[3]Chiaverini, M. J., Malecki, M. J., Sauer, J. A., Knuth, W. H., and Majdalani, J., "Vortex Thrust Chamber Testing and Analysis for O2-H2 Propulsion Applications," AIAA Paper 2003-4473, July 2003.

[4]Matveev, I., Matveeva, S., and Serbin, S., "Design and Preliminary Test Results of the Plasma Assisted Tornado Combustor," AIAA Paper 2007-5628, July 2007.

[5]Penner, S. S., "Elementary Considerations of the Fluid Mechanics of Tornadoes and Hurricanes," *Acta Astronautica*, Vol. 17, 1972, pp. 351-362.

[6]Königl, A., "Stellar and Galactic Jets: Theoretical Issues," *Canadian Journal of Physics*, Vol. 64, 1986, pp. 362-368.

[7]Kirshner, R. P., *The Extravagant Universe: Exploding Stars, Dark Energy, and the Accelerating Cosmos*, Princeton University Press, Princeton, New Jersey, 2004.

[8]Reydon, R. F., and Gauvin, W. H., "Theoretical and Experimental Studies of Confined Vortex Flow," *The Canadian Journal of Chemical Engineering*, Vol. 59, 1981, pp. 14-23.

[9]ter Linden, A. J., "Investigations into Cyclone Dust Collectors," *Proceedings of the Institution of Mechanical Engineers*, Vol. 160, 1949, pp. 233-251.

[10]Kelsall, D. F., "A Study of Motion of Solid Particles in a Hydraulic Cyclone," *Transactions of the Institution of Chemical Engineers*, Vol. 30, 1952, pp. 87-103.

[11]Smith, J. L., "An Experimental Study of the Vortex in the Cyclone Separator," *Journal of Basic Engineering-Transactions of the ASME*, 1962, pp. 602-608.

[12]Smith, J. L., "An Analysis of the Vortex Flow in the Cyclone Separator," *Journal of Basic Engineering-Transactions of the ASME*, 1962, pp. 609-618.

[13]Fontein, F. J., and Dijksman, C., *Recent Developments in Mineral Dressing*, Institution of Mining and Metallurgy, London, 1953, p. 229.

[14]Bloor, M. I. G., and Ingham, D. B., "Theoretical Investigation of the Flow in a Conical Hydrocyclone," *Transactions of the Institution of Chemical Engineers*, Vol. 51, No. 1, 1973, pp. 36-41.

[15]Bloor, M. I. G., and Ingham, D. B., "The Flow in Industrial Cyclones," *Journal of Fluid Mechanics*, Vol. 178, No. 1, 1987, pp. 507-519.

[16]Hsieh, K. T., and Rajamani, R. K., "Mathematical Model of the Hydrocyclone Based on Physics of Fluid Flow," *AIChE Journal*, Vol. 37, No. 5, 1991, pp. 735-746.

[17]Hoekstra, A. J., Van Vliet, E., Derksen, J. J., and Van den Akker, H. E. A., "Vortex Core Precession in a Gas Cyclone," *Advances in Turbulence, VII*, edited by U. Frisch, Kluwer, Dordrecht, The Netherlands, 1998, pp. 289-292.

[18]Hoekstra, A. J., Derksen, J. J., and Van den Akker, H. E. A., "An Experimental and Numerical Study of Turbulent Swirling Flow in Gas Cyclones," *Chemical Engineering Science*, Vol. 54, No. 13, 1999, pp. 2055-2065.

[19]Derksen, J. J., and Van den Akker, H. E. A., "Simulation of Vortex Core Precession in a Reverse-Flow Cyclone," *AIChE Journal*, Vol. 46, No. 7, 2000, pp. 1317-1331.

[20]Fang, D., Majdalani, J., and Chiaverini, M. J., "Simulation of the Cold-Wall Swirl Driven Combustion Chamber," AIAA Paper 2003-5055, July 2003.

[21]Rom, C. J., Anderson, M. H., and Chiaverini, M. J., "Cold Flow Analysis of a Vortex Chamber Engine for Gelled Propellant Combustor Applications," AIAA Paper 2004-3359, July 2004.

[22]Murray, A. L., Gudgen, A. J., Chiaverini, M. J., Sauer, J. A., and Knuth, W. H., "Numerical Code Development for Simulating Gel Propellant Combustion Processes," JANNAF Paper (unclassified), May 2004.

[23]Hu, L. Y., Zhou, L. X., Zhang, J., and Shi, M. X., "Studies of Strongly Swirling Flows in the Full Space of a Volute Cyclone Separator," *AIChE Journal*, Vol. 51, No. 3, 2005, pp. 740-749.

[24]Zhiping, Z., Yongjie, N., and Qinggang, L., "Pressure Drop in Cyclone Separator at High Pressure," *Journal of Thermal Science*, Vol. 17, No. 3, 2008, pp. 275-280.

[25]Molina, R., Wang, S., Gomez, L., Mohan, R., Shoham, O., and Kouba, G., "Wet Gas Separation in Gas-Liquid Cylindrical Cyclone Separator," *Journal of Energy Resources Technology*, Vol. 130, No. 4, 2008, p. 042701.

[26]Cortes, C., and Gil, A., "Modeling the Gas and Particle Flow inside Cyclone Separators," *Progress in Energy and Combustion Science*, Vol. in Press, 2007.

[27]Vatistas, G. H., Jawarneh, A. M., and Hong, H., "Flow Characteristics in a Vortex Chamber," *The Canadian Journal of Chemical Engineering*, Vol. 83, No. 6, 2005, pp. 425-436.

[28]Vyas, A. B., Majdalani, J., and Chiaverini, M. J., "The Bidirectional Vortex. Part 1: An Exact Inviscid Solution," AIAA Paper 2003-5052, July 2003.

[29]Vyas, A. B., and Majdalani, J., "Exact Solution of the Bidirectional Vortex," *AIAA Journal*, Vol. 44, No. 10, 2006, pp. 2208-2216.

[30]Vyas, A. B., Majdalani, J., and Chiaverini, M. J., "The Bidirectional Vortex. Part 2: Viscous Core Corrections," AIAA Paper 2003-5053, July 2003.

[31]Vyas, A. B., Majdalani, J., and Chiaverini, M. J., "The Bidirectional Vortex. Part 3: Multiple Solutions," AIAA Paper 2003-5054, July 2003.

[32]Majdalani, J., and Vyas, A. B., "Rotational Axisymmetric Mean Flow for the Vortex Injection Hybrid Rocket Engine," AIAA Paper 2004-3475, July 2004.

[33]Majdalani, J., “Vortex Injection Hybrid Rockets,” *Fundamentals of Hybrid Rocket Combustion and Propulsion*, edited by K. Kuo and M. J. Chiaverini, AIAA Progress in Astronautics and Aeronautics, Washington, DC, 2007, pp. 247-276.

[34]Vyas, A. B., and Majdalani, J., “Characterization of the Tangential Boundary Layers in the Bidirectional Vortex Thrust Chamber,” AIAA Paper 2006-4888, July 2006.

[35]Batterson, J. W., and Majdalani, J., “On the Boundary Layers of the Bidirectional Vortex,” AIAA Paper 2007-4123 June 2007.

[36]Maicke, B. A., and Majdalani, J., “A Constant Shear Stress Core Flow Model of the Bidirectional Vortex,” *Proceedings of the Royal Society, London, Series A*, Vol. 465, No. 2103, 2009, pp. 915-935.

[37]Majdalani, J., and Rienstra, S. W., “On the Bidirectional Vortex and Other Similarity Solutions in Spherical Coordinates,” *Journal of Applied Mathematics and Physics (ZAMP)*, Vol. 58, No. 2, 2007, pp. 289-308.

[38]Majdalani, J., Fang, D., and Rienstra, S. W., “On the Bidirectional Vortex and Other Similarity Solutions in Spherical Geometry,” AIAA Paper 2004-3675, July 2004.

[39]Hill, M. J. M., “On a Spherical Vortex,” *Philosophical Transactions of the Royal Society, London, Series A*, Vol. 185, 1894, pp. 213-245.

[40]Bragg, S. L., and Hawthorne, W. R., “Some Exact Solutions of the Flow through Annular Cascade Actuator Disks,” *Journal of the Aeronautical Sciences*, Vol. 17, No. 4, 1950, pp. 243-249.

[41]Barber, T. A., and Majdalani, J., “Exact Eulerian Solution of the Conical Bidirectional Vortex,” AIAA Paper 2009-5306, August 2009.

[42]Batchelor, G. K., *An Introduction to Fluid Dynamics*, Cambridge University Press, Cambridge, 1967.

[43]Gimbun, J., Chuah, T. G., Fakhru'l-Razi, A., and Choong, T. S., “The Influence of Temperature and Inlet Velocity on Cyclone Pressure Drop: A CFD Study,” *Chemical Engineering and Processing*, Vol. 44, 2005, pp. 7-12.

[44]Patankar, S. V., *Numerical Heat Transfer and Fluid Flow*, Hemisphere, Washington, D.C., 1980.

[45]Piomelli, U., Moin, P., and Ferziger, J. H., “Model Consistency in Large Eddy Simulation of Turbulent Channel Flows,” *Physics of Fluids*, Vol. 31, 1988, p. 1884.

[46]Vatistas, G. H., Lin, S., and Kwok, C. K., “Theoretical and Experimental Studies on Vortex Chamber Flows,” *AIAA Journal*, Vol. 24, No. 4, 1986, pp. 635-642.

[47]Vatistas, G. H., Lin, S., and Kwok, C. K., “Reverse Flow Radius in Vortex Chambers,” *AIAA Journal*, Vol. 24, No. 11, 1986, pp. 1872-1873.

[48]Fang, D., Majdalani, J., and Chiaverini, M. J., “Hot Flow Model of the Vortex Cold Wall Liquid Rocket,” AIAA Paper 2004-3676, July 2004.

[49]Truesdell, C., *The Kinematics of Vorticity*, Indiana University Press, Bloomington, IN., 1954.

[50]Anderson, M. H., Valenzuela, R., Rom, C. J., Bonazza, R., and Chiaverini, M. J., “Vortex Chamber Flow Field Characterization for Gelled Propellant Combustor Applications,” AIAA Paper 2003-4474, July 2003.

[51]Chang, F., and Dhir, V. K., “Mechanisms of Heat Transfer Enhancement and Slow Decay of Swirl in Tubes with Tangential Injection,” *International Journal of Heat and Fluid Flow*, Vol. 16, No. 2, 1995, pp. 78-87.

[52]Wu, J. Z., Ma, H. Y., and Zhou, M. D., *Vorticity and Vortex Dynamics*, Springer, New York, 2006.

[53]Aris, R., *Vectors, Tensors and the Basic Equations of Fluid Mechanics*, Dover Publications, Mineala, NY, 1962.